
Wesleyan ♦ University

ALMA Observations of Molecular Gas Emission from a Protoplanetary Disk in the Orion Nebula Cluster

by

Samuel Meir Factor

Faculty Advisor: Dr. A. Meredith Hughes

A thesis submitted to the faculty of Wesleyan University
in partial fulfillment of the requirements for the degree of
Master of Arts in Astronomy

Middletown, Connecticut

May 2015

Acknowledgements

First I would like to thank Prof. Meredith Hughes for her tireless work as my research advisor and mentor. If it weren't for your amazing introductory astronomy course, I may not have found my way into the field of astronomy.

I would also like to thank the other members of my committee, Prof. Seth Redfield and Prof. Karin Öberg.

Many thanks go to Fred Ellis and also Tsampikos Kottos for their advising of my physics research. Thank you both for getting me started in science research.

Thank you to the Wesleyan astronomy community as a whole: professors, post docs, graduate students, and undergrads. The learning environment that every one of you contributes to is so special. Thank you specifically to the disk detectives, I'll be sad to leave. Thank you to Kevin, for all the work you did to get this project off the ground with the model and cluster, and to my office-mates, for all the encouragement and the occasional distraction.

Thank you to my parents for your constant support.

Thank you to Claire for putting up with all the late nights I spent at the observatory, you're the best! Also, thank you to my other house mates, Nick and Alyssa, for making the house a fun, stress-free environment.

Finally, I would like to thank Wesleyan University for computer time supported by the NSF under grant number CNS-0619508, and the Connecticut Space Grant Consortium for a travel grant which helped support my trip to the 225th meeting of the American Astronomical Society to present this work.

This work makes use of the following ALMA data: ADS/JAO.ALMA #2011.0.00028.S. ALMA is a partnership of ESO (representing its member states), NSF (USA) and NINS (Japan), together with NRC (Canada) and NSC and ASIAA (Taiwan), in cooperation with the Republic of Chile. The Joint ALMA Observatory is operated by ESO, AUI/NRAO and NAOJ. The National Radio Astronomy Observatory is a facility of the National Science Foundation operated under cooperative agreement by Associated Universities, Inc.

This work also makes use of molecular data made available by Schöier et al. (2005).

Contents

1	Introduction	1
1.1	The Minimum Mass Solar Nebula, a Fiducial Model	2
1.2	Submillimeter Observations	3
1.2.1	Interferometry	3
1.2.2	Continuum Emission	7
1.2.3	Molecular Gas Emission	8
1.3	Disks in Low-Mass Star Forming Regions	9
1.4	Disks in High-Mass Star Forming Regions	10
1.5	Previous Observations of d216-0939	12
2	Observations	16
3	Results	19
3.1	Minimization of Cloud Contamination	19
3.2	Line Data	20
4	Modeling	29
4.1	Gas Model	29
4.2	MCMC Methods	36
4.3	Fitting Procedure	39
4.3.1	$\text{HCO}^+(4-3)$ Fit	40
4.3.2	$\text{CO}(3-2)$ Fit	42
4.3.3	Combined Fit	46
4.4	Evaluation of the LTE Assumption	54
4.5	Elliptical Disk Model	54
5	Discussion	59
5.1	Planet-Forming Potential	59
5.2	Dynamical Mass of a Pre-Main Sequence Star	60
5.3	Best Fit Temperature Structure	65
5.4	HCO^+ Abundance Structure	66
5.5	Rough Characterization of Ionizing Radiation Level	68
5.6	High Velocity Asymmetry	70
6	Summary	75
References		77

List of Figures

1.1	Orion Disk Masses vs. Distance from θ^1 Ori C	12
1.2	Radio Continuum and Scattered Light Images from the Literature	13
2.1	Location of Observed Fields in Orion	17
3.1	HCO(4–3) Moment Maps	21
3.2	CO(3–2) Moment Maps	22
3.3	HCN(4–3) and CS(7–6) Moment Maps	22
3.4	CO(3–2) Channel Maps	26
3.5	HCO ⁺ (4–3) Channel Maps	27
3.6	HCO ⁺ (4–3) Position-Velocity Diagram	28
4.1	Typical Density and Temperature Structure	32
4.2	χ^2 Values for an MCMC Run	38
4.3	Triangle Plot from Fitting HCO ⁺ (4–3) Only	43
4.4	Residuals from Best Fit to HCO ⁺ Only	44
4.5	Triangle Plot from Fitting CO(3–2) Only	47
4.6	Residuals from Best Fit to CO Only	48
4.7	Triangle Plot from Fitting HCO ⁺ (4–3) and CO(3–2)	51
4.8	HCO ⁺ (4–3) Residuals from Best Fit to HCO ⁺ and CO Together	52
4.9	CO(3–2) Residuals from Best Fit HCO ⁺ and CO Together	53
4.10	Comparison of LTE model to Non-LTE model	55
4.11	Eccentric Disk Velocity Field and Surface Density	58
5.1	Best Fit Surface Density Profiles	61
5.2	Pre-Main Sequence Evolutionary Tracks	64
5.3	Best Fit Midplane Temperature Profile	67
5.4	Gravitational Instability Toomre Q Parameter	74

List of Tables

3.1	Integrated Flux Measurements	23
3.2	Gaussian Fits to Visibilities	24
4.1	Model Parameters	35
4.2	Best Fit Parameters to Individual Lines	42
4.3	Best Fit Parameters to Both Lines	49

Chapter 1

Introduction

Planetary systems like our own are born from circumstellar disks. The properties of such disks can give us insight into the conditions under which planets form and the physics behind that process. Protoplanetary disks are young (typically $\lesssim 10$ Myr) circumstellar disks containing dust *and* gas which form due to conservation of angular momentum and thus are a natural side effect of star formation. As such they are common around young stars (Strom et al. 1989; Weintraub et al. 1989; Beckwith et al. 1990).

Disk around young stars are easily identified by their “infrared excess.” The cool dust that makes up $\sim 1\%$ of the disk mass gives off thermal emission, which peaks in the infrared. This excess is easily seen in the spectral energy distribution (SED) of the combined star and disk system. An SED plots the energy emitted by a source (expressed as λF_λ or νF_ν) as a function of wavelength, λ , or frequency, ν .

Protoplanetary disks tend to have a flared structure with radii up to a few hundred AU (Vicente & Alves 2005), temperatures in the outer disk between 10–100 K, and disk masses from $\lesssim 0.001$ to $\sim 0.1 M_\odot$ ($\sim 1 - 100 M_{\text{Jupiter}}$, Andrews & Williams 2005). Gaseous disks tend to live for a few Myr ($\lesssim 10$, Hernández et al. 2008) after which the gas disperses and leaves behind a debris disk. Debris disks are made up of what is thought to be second generation dust, generated by collisions between large bodies, as first generation dust would be removed by radiation pressure on timescales much shorter than the stellar age. They also contain no gas, with a few interesting exceptions (e.g. 49 Ceti, Hughes

et al. 2008a). For an in-depth review of protoplanetary disk evolution covering the transformation from protoplanetary disks to debris disks which is beyond the scope of this work, see Williams & Cieza (2011).

1.1 The Minimum Mass Solar Nebula, a Fiducial Model

One of the most exciting reasons to study protoplanetary disks is to discover the origins of exoplanetary systems. We use our own solar system as a yardstick for planet-formation potential in other systems using a theoretical protoplanetary disk, called the minimum mass solar nebula (MMSN, Weidenschilling 1977). The MMSN is created by grinding up the mass in the solar system, adding light elements until solar abundances are reached, and spreading out that mass in between the next inferior and superior planets. We are then left with the minimum surface density profile of the protoplanetary disk, from which our own solar system formed.

Since we know that our solar system formed planets we can compare this disk to protoplanetary disks around other stars to gauge their planet-forming potential. However, the MMSN assumes that the planets formed in their current positions, which we now know may not be true (Walsh et al. 2011; Tsiganis et al. 2005). Planet migration can cause the host disk to loose mass, either through the scattering of planetesimals by passing planets, or the shepherding of planetesimals into the inner disk where they may be accreted onto the star (Izidoro et al. 2014). Migration can also rearrange mass in the disk. Thus the MMSN is by no means the minimum mass *planet-forming* disk, though it does give us a baseline for how much mass would need to be available to form a planetary system like our own.

1.2 Submillimeter Observations

Submillimeter observations allow us to peer through the dust in the outer disk, which would be optically thick at shorter wavelengths, and detect emission from the disk interior. In the submillimeter regime we detect two types of emission. The first is continuum emission from thermally radiating dust particles. With spectrally resolved observations, we can also detect line emission from small molecules in the gas phase, which have rotational transitions in the radio frequency regime. These observations allow us to ascertain not only the total mass of the disk but also more subtle characteristics such as temperature and density structure. Noticeably absent is any emission from the central star, as its thermal emission is very weak at these wavelengths. A discussion of what each of these types of emission can tell us about the disk follows after a brief introduction to interferometry.

1.2.1 Interferometry

Interferometry is an extremely powerful tool which enables high resolution observations without the need for an extremely large aperture. With a conventional telescope (using a single mirror or dish), the resolution is limited by diffraction caused by the edges of the aperture given by

$$\theta = 1.22 \frac{\lambda}{D}, \quad (1.1)$$

where θ is the diffraction limited resolution (in radians), λ is the wavelength of observation, and D is the diameter of the aperture. Since the wavelength in the radio frequency domain is so large the resolution is proportionally coarse. For

example the Arecibo Observatory, the largest single aperture telescope in the world, has a maximum diffraction limited resolution of ~ 25 arcsec ($D=300$ m, $\lambda=3$ cm). While moving to shorter wavelengths does help, large apertures are more difficult to build due to the higher tolerances required in manufacturing reflecting surface used for shorter wavelengths. For example, the James Clark Maxwell Telescope has a diffraction limited resolution of ~ 7.5 arcsec ($D=15$ m, $\lambda=450$ μm). This is not nearly high enough resolution to resolve detailed structure in protoplanetary disks. Thus we must find a way to increase the resolution without increasing the size of the dish.

This is where we turn to interferometry. We can use two or more separate telescopes and interfere the light from them to reconstruct an image. This image now has a diffraction limited resolution (synthesized beam) set by the separation between the telescopes (or baseline) and a field of view (primary beam) set by the diffraction limit of each telescope. While interferometry is possible when using CCD detectors, it is extremely difficult as light must be physically combined from two separate telescopes before it is imaged. Interferometry is much easier to perform when heterodyne receivers are used. This is due to the fact that receivers not only detect the amplitude, or intensity, of incident radiation, but also the phase. Amplitude and phase information can then be correlated by a supercomputer to digitally interfere signals from multiple antennae.

Maintaining phase information is crucial. With extremely precise measurements of baseline lengths we can remove the phase delay caused by the physical separation of the two telescopes, along the line of sight to the source. Atmospheric and instrumental phase delays must also be calibrated out.

Baselines are often referred to by their coordinates in the uv plane. The uv plane is a wavelength scaled $x - y$ coordinate system parallel to the sky in the

direction of the source of interest. In other words, $u = X/\lambda$ and $v = Y/\lambda$, where λ is the wavelength of observation and X and Y are the lengths of the x/y components of the projected baseline. In this way each baseline samples a specific spatial frequency determined by its position in the uv plane. The complex voltage (amplitude and phase) obtained by interfering signals from two separate telescopes, combined with that baseline's position in the uv plane is called a visibility. With enough visibilities, sampling a wide variety of spatial frequencies (or points in the uv plane), we can begin to reconstruct an image. We can also use the earth's rotation to move the antennas, in the plane of the sky, to fill in points in the uv plane by observing a source at intervals throughout a night. This is called "earth rotation aperture synthesis". Ideally we would have an infinite number of telescopes such that the uv plane would be completely filled in. In this case the image would be simply the Fourier transform of the visibilities. Unfortunately this is impossible and we must settle for incomplete uv coverage. Since we are only sampling a finite number of spatial frequencies, the true image cannot be recovered. In other words, an infinite number of images could be constructed which would fit any finite set of visibilities (though many are not physically possible).

To determine the angular resolution, or synthesized beam, of an interferometer, just like any other type of telescope, we consider the shape of the image produced when observing a point source (or delta function). Since the Fourier transform of a delta function is a constant, this is simply the Fourier transform of the points in the uv plane sampled by the baselines, assuming zero phase and an amplitude of 1 for each visibility. For a conventional telescope, this is an Airy disc, the 2-D Fourier transform of a filled circle (the uv coverage of the primary mirror). The synthesized beam for an interferometer can be complicated for an under-sampled uv plane, but with adequate uv coverage it can begin to look like a bumpy and/or

elongated Airy disk. This reduces artifacts introduced in the imaging process.

The Fourier transformation of the visibilities is the convolution of the dirty beam and the sky brightness distribution. An irregular synthesized beam can introduce artifacts which are not present in the true sky image, such as areas with negative intensity, which we would like to minimize or remove. This process is called deconvolution. Two methods of deconvolution have been widely used. The first and most popular is the CLEAN algorithm presented by Högbom (1974). It assumes that the image consists of point sources. The *dirty beam* (or raw synthesized beam) is iteratively subtracted from the *dirty map* (the Fourier transform of the visibilities) at the point of peak intensity, while keeping track of the position of these points in the *clean component map*. This is done until a noise threshold is reached or a predetermined number of point sources has been subtracted. An elliptical Gaussian is then fit to the *dirty beam* generating the *clean beam*. The image is reconstructed by convolving the *clean beam* with the *clean component map* and adding the final residuals from the *dirty map*. We use the CLEAN algorithm in this work. A second, less popular, image deconvolution algorithm is the maximum entropy method (MEM). This algorithm essentially chooses the smoothest image which fits the visibilities to within the noise level. Many algorithms have been published for solving this problem (Wernecke & D'Addario 1977; Skilling & Bryan 1984; Cornwell & Evans 1985).

The Atacama Large Millimeter/submillimeter Array (ALMA) is the most powerful submillimeter interferometer ever built. When completed, it will host 50 12 m and 16 7 m antennae. Baselines will extend out to 15 km. This represents an order of magnitude increase in both sensitivity and resolution over previous arrays. With this new capability, not only will it be possible to study nearby disks on the \sim AU scale (ALMA Partnership et al. 2015) but also disks which were previously

marginally or even unresolved, such as d216-0939, in greater detail.

1.2.2 Continuum Emission

One of the most important characteristics of a disk, in terms of planet-formation potential, is its mass. Assuming that the continuum emission is optically thin, the flux density, F_ν , is directly proportional to the disk mass, M_{disk} (Hildebrand 1983) according to

$$M_{\text{disk}} = \frac{d^2 F_\nu}{\kappa_\nu B_\nu(T_c)} \quad (1.2)$$

where d is the distance to the source, κ_ν is an assumed dust opacity, and $B_\nu(T_c)$ is the Planck function at an assumed characteristic temperature T_c . This method relies on some assumptions which may not always be true including optically thin emission, a single temperature throughout the disk, and a single dust opacity throughout the disk (based on assumptions of the composition and grain sizes). Most important, is the assumption of a dust-to-gas ratio of 1:100 (contained in the normalization of κ_ν), assumed to be the same as the interstellar medium. Williams & Best (2014) demonstrated that the assumption of a 100:1 gas-to-dust ratio may not always be valid. With multi-wavelength fitting of a disk's SED using a simple model, one can infer a characteristic temperature and opacity power law index (associated with the grain size distribution). The assumption of optically thin emission results in these calculations inherently being lower limits, since any substantial optical depth will effectively hide emission from the disk interior. This is enhanced by the fact that a substantial amount of mass might already be locked up in bodies larger than the wavelength of observation which are essentially invisible in the submillimeter.

1.2.3 Molecular Gas Emission

A more direct way to measure the mass of a disk is to observe the gas, as it makes up the vast majority of material in the disk at this stage. As H₂, the dominant constituent, is a symmetric molecule (has no permanent dipole moment) and thus rotational transitions are forbidden, it cannot be observed in the sub-millimeter. Instead, we observe CO, the second most abundant molecule and is thus exhibits the brightest line emission. We can also observe other molecules including HCO⁺, HCN, CS, CN and others including their isotopologues. Since the level populations, and thus the relative intensity of line emission, are coupled to the temperature of the disk, we no longer need to assume a temperature. With multiple lines or a single optically thick line, we can model it.

In an optically thin line, brighter emission may be caused by a higher temperature or density. Thus, there is a degeneracy between these two properties. Optically thick emission, since it originates from the $\tau = 1$ surface and thus a single temperature does not exhibit this degeneracy, though only gives us a single point in the vertical temperature structure. Thus multi-line observations are needed to accurately constrain both the temperature and the density structure.

If we want to estimate a total gas mass (which is assumed to be the disk mass as dust mass is insignificant), we must assume a fractional abundance of the gas species observed. This is similar to the assumption of a gas-to-dust ratio, in that we need to convert the mass we measure of a specific species into a total disk mass. Once again this is mainly an assumption based on the values of the ISM or chemical simulations. For example, we assume the fractional abundance of CO is 10⁻⁴, the same as the value for a warm dense cloud (e.g. Aikawa & Herbst 1999; Fogel et al. 2011). For other species that exhibit more complicated

chemistry, we can use a combination of values from the ISM and from chemical simulations of disks (e.g. Cleeves et al. 2014; Walsh et al. 2013). These values may not be constant with location or age. Bergin et al. (2013) demonstrated this by comparing observations of HD in TW Hya to models from the literature made from observations of CO.

1.3 Disks in Low-Mass Star Forming Regions

Spatially and spectrally resolved observations and subsequent modeling of nearby circumstellar disks have allowed us to accurately characterize many aspects of their structure. Observations of dust continuum emission from disks in the nearby star-forming regions (SFRs) of Taurus-Auriga and ρ Ophiuchus by Andrews & Williams (2005, 2007) have yielded a wide distribution of disk masses with a median of $0.005 M_{\odot}$. A large fraction of the surveyed disks are more massive than the MMSN of roughly $0.01 M_{\odot}$ (Weidenschilling 1977). This indicates that disks with planet-forming potential are common, in accordance with our observations of richness of exoplanetary systems discovered by the Kepler mission and other planet finding surveys (Fressin et al. 2013).

These and other studies using high resolution observations of nearby disks (Andrews et al. 2009, 2010; Isella et al. 2009) have allowed us to develop our parameterization of disk temperature and density structure. Thus, when we observe and model more distant disks (e.g. disks in Orion) which are resolved in less detail, we already have a set of models (described fully in Section 4.1) that are grounded in observations.

1.4 Disks in High-Mass Star Forming Regions

Most previous submillimeter studies have focused on the low-mass SFRs of Taurus-Auriga and ρ Ophiuchus due to the limited sensitivity and angular resolution of submillimeter interferometers. While these studies do show that disks with planet-forming potential seem to be common, they do not tell the whole story.

Most stars form in massive, dense clusters (*high-mass* SFRs, Lada & Lada 2003), environments extraordinarily different from previously studied *low-mass* SFRs. These regions host more high-mass O and B stars, which give off ionizing radiation, and a higher density of stars, increasing the chance of gravitational interaction. Both of these features of high-mass SFRs cause mass loss in protoplanetary disks which could hinder planet formation.

The Hubble Space Telescope (HST) has observed the Orion Nebula Cluster (ONC), the closest of these high-mass SFRs, and produced a plethora of images showing protoplanetary disks surrounded by tear-drop-shaped shells (dubbed “proplyds”) pointing away from θ^1 Ori C (Spectral type O6, O’dell & Wen 1994; McCullough et al. 1995; Bally et al. 1998; Smith et al. 2005; Ricci et al. 2008). These images beautifully show the harsh environment created by the nearby O star and indicate that it may have an effect on the evolution of protoplanetary disks. Separate observations by Churchwell et al. (1987), using the VLA, and Henney & O’Dell (1999), using Keck, have measured mass loss rates of $\dot{M} \approx 10^{-7} M_{\odot}$ yr $^{-1}$. Such a substantial mass loss rate would disperse a typical disk before giant planets could form (Hubickyj et al. 2005), and is in apparent contradiction with the inferred ages of the disk-hosting ONC stars (\sim 2 Myr, Reggiani et al. 2011; Da Rio et al. 2009). Thus, we would like to gain a better understanding of the effects of environment on protoplanetary disks and compare disks in these

regions, which would be more typical of the general disk population, to disks we have previously studied in low-mass SFRs.

Another reason to study disks in these regions is a little closer to home. There is evidence indicating that our solar system formed in a high-mass SFR. Tachibana et al. (2006) supported this hypothesis using meteoritic levels of ^{60}Fe , a short-lived isotope of iron that can only be formed in stars. From the measured ratio of $^{60}\text{Fe}/^{56}\text{Fe}$ in chondrules, they infer the ratio when the solar system formed. They then compare this value to predicted ratios produced by nucleosynthesis in different types of stars. They find that a nearby supernova is the most probable source of this and other radionucleotides in the early solar system. This event indicates that our sun formed in a region with a high rate of star formation with a broad spectrum of masses, typical of a high-mass SFR and not possible in a low-mass SFRs. Gaidos et al. (2009) use levels of ^{26}Al to support this hypothesis though they attribute the levels they see to winds generated by nearby high-mass stars.

All previous disk masses in the ONC have been determined based on observations of millimeter continuum emission from dust. Surveys using the Submillimeter Array (SMA) by Mann & Williams (2009a,b, 2010) have shown that the upper end of the disk mass distribution is truncated in the ONC and there is a positive correlation of disk mass with distance from $\theta^1\text{ Ori C}$. Observations by Mann et al. (2014) using the Atacama Large Millimeter/submillimeter Array (ALMA) have confirmed these results with a probability of no correlation of $< 10^{-4}$ (see Figure 1.1). They attribute this trend to external photoevaporation since stellar interactions remove relatively small amounts of mass. They also note that despite the observed disk destruction, the region shows similar potential for planet-formation to that of low-mass SFRs, with 30% of surveyed disks having masses greater than

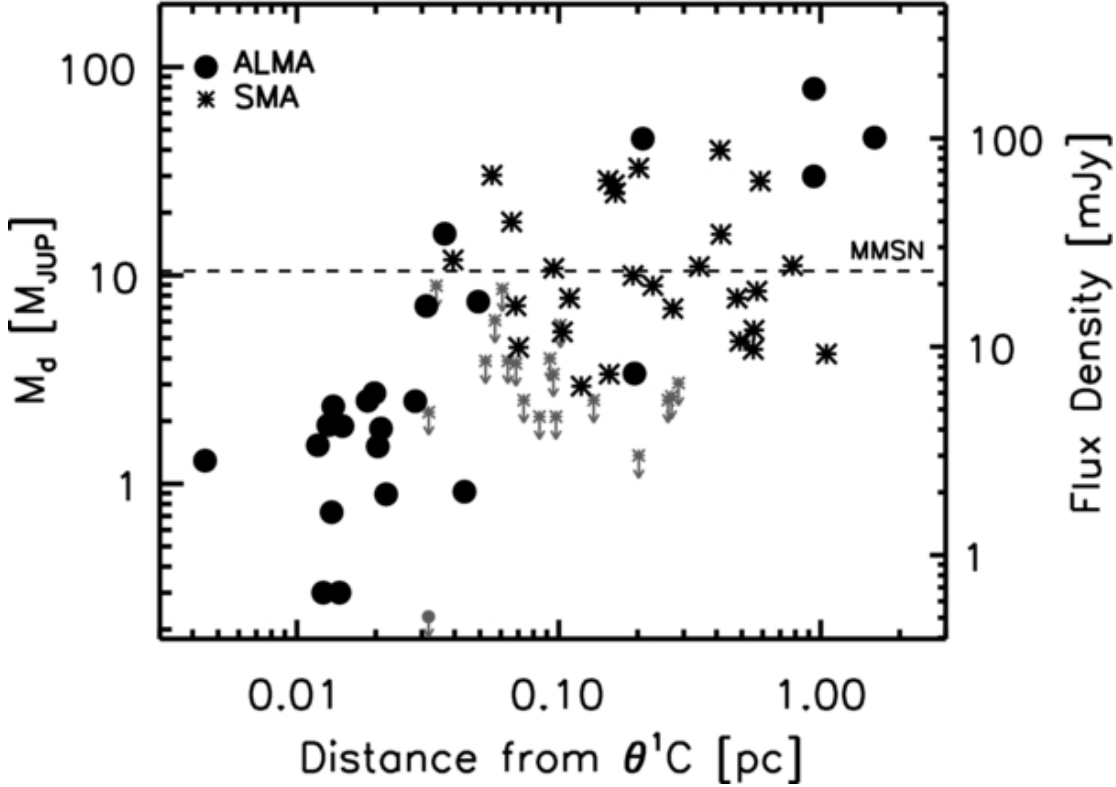


Figure 1.1: Circumstellar continuum derived disk masses versus their projected distance from θ^1 Ori C. Dots represent disks from Mann et al. (2014), while stars represent from Mann & Williams (2010). Observations were made using ALMA and the SMA respectively. Small grey symbols with arrows represent 3σ upper limits on disks observed but not detected. The dashed line represents the MMSN disk mass. Figure reproduced from Mann et al. (2014).

or equal to the MMSN. For comparison, $\sim 37\%$ and 29% of disks in Taurus and ρ Ophiuchus respectively have derived disk masses greater than or equal to the MMSN Andrews & Williams (2005, 2007). The effects of environment on the structure and chemistry of gas in protoplanetary disks have yet to be measured.

1.5 Previous Observations of d216-0939

The subject of this work is d216-0939 (proplyd designation based on the nomenclature of O'dell & Wen 1994, derived from the source's RA and Dec coor-

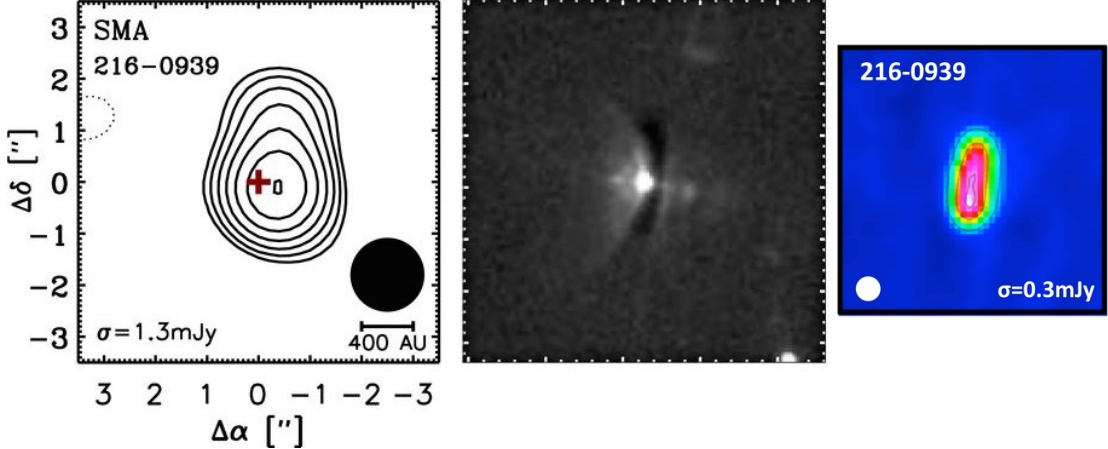


Figure 1.2: Previous observations of d216-0939 shown at the same scale. From left to right, the images show SMA $880\text{ }\mu\text{m}$ continuum observations from Mann & Williams (2009a) (contours begin at the 5σ level and each step is an increase in intensity by a factor of 1.5), the HST H α discovery image from Smith et al. (2005), and ALMA $856\text{ }\mu\text{m}$ continuum observations from Mann et al. (2014). The synthesized beam of the continuum observations is shown in the lower right/left corner along with the rms noise level.

dinates), a pre-main-sequence star with a spectral type of K5 (Hillenbrand 1997) located in the outskirts of the Orion Nebula (projected distance 1.6 pc, Mann et al. 2014, see Figure 2.1). Figure 1.2 shows images of the disk taken directly from the work referenced in the following discussion.

The disk was discovered by Smith et al. (2005) using HST and is one of the largest and most massive disks in the ONC (Mann & Williams 2009a, 2010; Mann et al. 2014). Smith et al. (2005) determined that the disk is almost edge-on with an inclination of $\sim 80^\circ - 75^\circ$ to the east¹ and a position angle of 173° (E of N). They also noted that the northern portion of the disk, as seen in scattered light, is $\sim 50\%$ larger than the southern portion. The disk is also associated with HH 667 E, a partial bow shock slightly bent to the south, and HH 667 W, several diffuse

¹This value is derived from the fact that the line of sight to the star is very close to the flared surface of the disk. They report the inclination with respect to the disk axis rather than with respect to the plane of the disk and thus report a value of $\sim 10^\circ - 15^\circ$.

filaments along the rotation axis of the disk.

Continuum observations using the SMA by Mann & Williams (2009a) have marginally resolved the disk and determined its mass to be $0.0450 \pm 0.0006 M_{\odot}$ with a radius of 291 AU. They detected no signs of external photoevaporation, as would be expected from its location far away from any O or B stars. Analysis of continuum data from ALMA (from which gas line data is presented here) by Mann et al. (2014) produced a disk mass of $0.0437 \pm 0.0007 M_{\odot}$ with a radius of 525 AU. Mann & Williams (2009a) also strongly detected the CO(3–2) transition but were unable to separate the disk from the cloud contamination.

Using observations from the Combined Array for Research in Millimeter Astronomy (CARMA) and the Australia Telescope Compact Array (ATCA), Ricci et al. (2011) were able to fit the long wavelength spectral index to determine a dust opacity index of $\beta = 1.0 \pm 0.3$, indicative of grain growth. The dust opacity is assumed to be a power law as a function of frequency: $\kappa_{\nu} \propto \nu^{\beta}$. They also derive a disk mass of $0.02 M_{\odot}$.

With our high resolution observations of gas line emission, we aim to better constrain the mass, as well as determine the temperature and density structure of d216-0939 and the mass of the host star. With this information we will examine this disk, located in the outskirts of the ONC, in the context of previously studied protoplanetary disks located in Taurus and Ophiuchus and compare the planet-forming potential. We also obtain a dynamical mass measurement for this pre-main sequence star which can be compared to theoretical evolutionary tracks. This work is organized as follows: The observations and data reduction are described in Chapter 2. Data are presented in Chapter 3 along with basic metrics and rudimentary analysis. Modeling and MCMC fitting techniques are discussed and best fit models are presented in Chapter 4. Best fit parameters are discussed in

Chapter 5 along with a discussion of an interesting feature we observed in this disk.

Chapter 2

Observations

Data presented here are part of an ALMA survey of the Orion proplyds (project 2011.0.00028.S). Mann et al. (2014) performed analysis of the dust continuum data for all detected sources, while the gas line emission from d216-0939 is described in this work. This survey consisted of 5 pointings (or Fields) shown in Figure 2.1, two covering the crowded region near the Trapezium cluster and three targeting more isolated disks. The observations were made on October 24, 2012, using the Band 7 (345 GHz) receivers. Four 1.875 GHz-wide spectral windows were arranged to cover the HCO⁺(4–3), HCN(4–3), CO(3–2), and CS(7–6) emission lines at 356.734, 354.505, 345.796, and 342.883 GHz respectively (around 850 μm). Each window was divided into 3840 channels each with a width of 488.28 kHz corresponding to a velocity resolution of 0.42 km/s. For this Cycle 0 Early Science project, 22 of the eventual 50 12m antennas were online in a hybrid configuration with baselines ranging from 21.2 to 384.2 m. This results in a largest recoverable scale of 5 arcsec and an angular resolution of 0.5 arcsec. Later, baselines shorter than $70k\lambda$ were excluded to minimize large scale cloud contamination, resulting in a largest recoverable scale of 3.6 arcsec (see Section 3.1 for further discussion of this procedure). The 12 m diameter antennas produce a primary beam FWHM of 15 arcsec. The data presented here, from Field 5 of Mann et al. (2014), represent 22 minutes of on-source time, achieving an rms of 0.5 mJy/beam in the continuum and 6 mJy/beam in the line observations. Observations were spaced out over 7.5 hours to ensure adequate uv coverage and resulted in a synthesized beam (angular resolution) of 0.57×0.52 arcsec with a position angle of 88.8° using

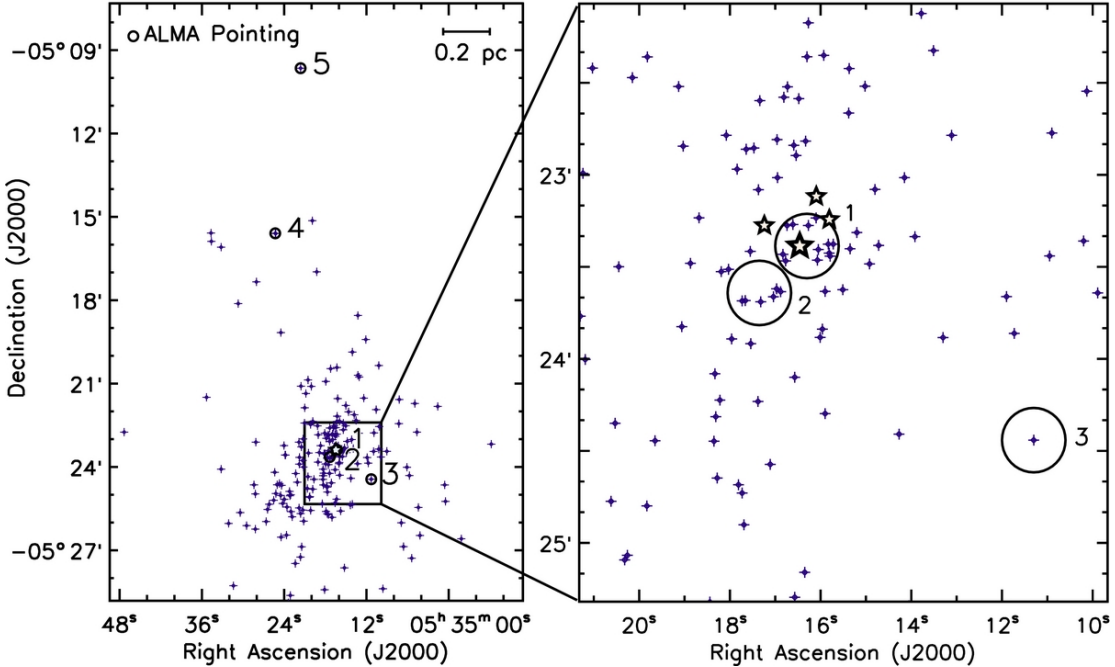


Figure 2.1: Location of the fields observed by ALMA in the Orion Nebula Cluster. The stars mark the position of the OB stars, and crosses mark the location of proplyds identified by HST observations (Ricci et al. 2008). Black circles represent the primary beam of the ALMA observations. Our target of interest, d216-0939, is located in field 5. Figure reproduced from Mann et al. (2014).

natural weighting. When excluding baselines shorter than $70k\lambda$ the synthesized beam was 0.51×0.47 arcsec with a position angle of 89.5° . Precipitable water vapor in the atmosphere was stable around 0.7 mm.

Data calibration was performed by ALMA staff using the standard procedures in the CASA package. The antenna-based complex gains and bandpass response of the system were calibrated using observations of the quasars J0607-085 and J0522-364 respectively. The complex gain calibration for a radio interferometer is essentially using a standard star, or in this case a quasar, to correct for long term atmospheric and instrumental gain variations. Any variations in the amplitude or phase (which should be 0 for a point source such as a quasar) of the calibrator are modeled and removed from the observations of the source of interest. The

bandpass calibration is similar to the flat field calibration done with a CCD, only in the spectral domain rather than the spatial; it is done once per observing run to correct for the non-uniform response of the receiver and correlator across the sampled channels in the spectrum. The absolute flux calibration, which sets the conversion between the output voltage of the receiver to brightness temperature or flux density, was determined from observations of Callisto. These observations are then compared to a model of the source which gives the expected temperature or flux density. These models are accurate to $\sim 10 - 20\%$ due to uncertainties in the surface properties of the planet or moon. The model of Callisto was that provided by Butler (2012).

The velocity reference frame was changed from the ALMA standard topocentric to LSRK (kinematical local standard-of-rest) using the CASA task `cvel`. Continuum subtraction in the visibility domain was performed and channels containing line data were split out, excluding baselines shorter than $70 \text{ k}\lambda$ in order to minimize large angular scale cloud contamination while maintaining good signal to noise ratio (this was done in CASA). Visibilities were then inverted, using a natural weighting, deconvolved using the clean algorithm and restored using the standard procedures in the MIRIAD package.

Chapter 3

Results

Spatially and spectrally resolved line emission was detected for CO(3–2), HCO⁺(4–3), HCN(4–3), and CS(7–6) across approximately 40 channels with a channel width of 0.41 km/s in CO(3–2) and 0.42 km/s in HCO⁺(4–3). Moment maps, channel maps, and line statistics are presented here after a short discussion of cloud contamination.

3.1 Minimization of Cloud Contamination

Cloud contamination occurs when emission from background or foreground gas clouds is detected along with the source you are observing. In some cases the cloud contamination can be indistinguishable from the target source. This was the case in observations of d216-0939 using the SMA by Mann & Williams (2009a); CO(3–2) was strongly detected but the disk could not be distinguished from the contamination. In that case, their main focus was analysis of the dust continuum, so they simply excluded channels with CO contamination. In observations with lower spectral resolution, this is not possible; when analyzing the dust continuum a correction factor must be applied to account for the extra flux (e.g. Drabek et al. 2012). As the Orion nebula is a denser region of space than the low-mass SFR’s of Taurus and Ophiuchus, cloud contamination is much more common and must be dealt with. In our high resolution observations from ALMA, we can distinguish the disk from the cloud contamination. Even so, an effort must be made to minimize the contamination so that it does not interfere with the fitting

procedure.

One way minimize cloud contamination is to exclude short baselines from the dataset. Just as the long baselines control the angular resolution, or *smallest* recoverable scale, the short baselines control the *largest* recoverable scale. As cloud contamination tends to be large scale in nature, excluding short baselines reduces its contribution to the observations, essentially resolving it out. While this process slightly reduces the total observed flux from the disk, it is necessary in order to remove irrelevant emission which may hinder the fitting procedure. This spatial filtering illustrates the power of interferometry over conventional telescopes. While increasing the diameter of a conventional telescope increases its resolution, there is no way to decrease the largest recoverable scale short of aperture masking, which greatly reduces the detected flux.

We settled on a minimum baseline length by observing the HCO⁺ cloud to the south west of the disk steadily decrease in size as longer baselines were excluded. Excluding baselines shorter than $70k\lambda$ reduced the cloud contamination the most without reducing the flux from the disk enough to push it too close to the noise threshold.

3.2 Line Data

Moment maps are a simple way of visualizing a data cube (α, δ, ν) . Moment 0 is the integrated intensity as a function of position over all channels and moment 1 is the intensity-weighted velocity. Moment maps for HCO⁺(4–3) and CO(3–2) are shown in Figures 3.1 and 3.2 respectively, illustrating the effects of excluding short baselines to minimize cloud contamination. The field of view is slightly wider than the disk to include the contamination to the South-West. Even after

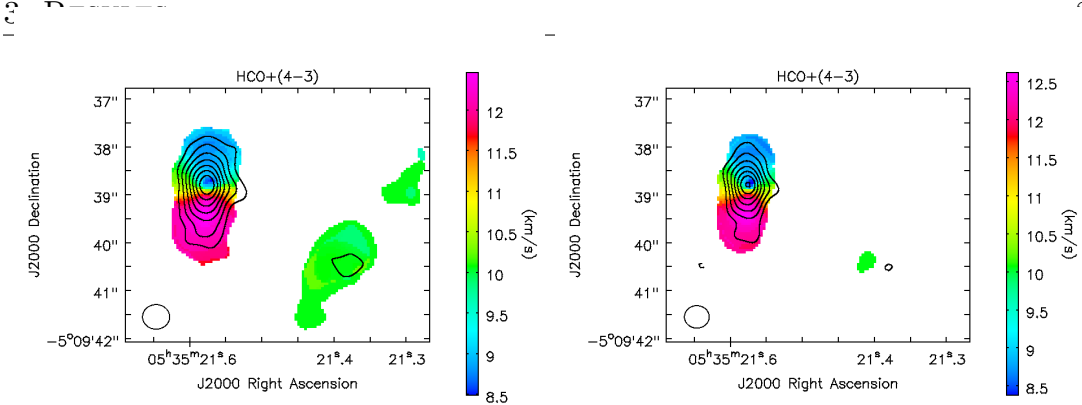


Figure 3.1: Integrated emission maps of the HCO(4–3) transitions including all baselines (left) and excluding all baselines shorter than $70k\lambda$ (right). Contours are integrated line emission at $3, 5, 7 \dots 15\sigma$ where 1σ is 32 and 28 mJy beam $^{-1}$ km s $^{-1}$ respectively. Colors show the intensity-weighted velocity (LSRK). The beam is shown in the bottom left corner. The beam diameter is 0.5 arcsec corresponding to 200 AU at this distance.

this procedure, the CO(3–2) emission is still highly contaminated. The HCO⁺(4–3) line, on the other hand, is almost free of contamination after excluding short baselines. Figure 3.3 shows moment maps for the HCN(4–3) and CS(7–6) emission. Although not modeled in this work, HCN is completely free of contamination without excluding short baselines. CS emission is detected at the 3σ level and only marginally resolved. In all maps, rotation is clearly visible as a transition from red-shifted emission in the south to blue-shifted in the north. The maximum extent of the 3σ contour along the disk major axis corresponds to an outer diameter of the HCO⁺ and HCN disks of 900 and 1050 AU respectively at a distance of 400 pc (CO and CS are too contaminated and not well resolved respectively).

Integrated line intensity above the 3σ level and elliptical Gaussian fits to the visibilities are given in Tables 3.1 and 3.2. We determined the integrated line intensity using the MIRIAD task `cgcurs` to measure the intensity in the zeroth moment map enclosed by the 3σ contour. Stated uncertainties on the integrated line intensity do not include the absolute flux calibration uncertainty of the ALMA observations of $\sim 10\%$ (Mann et al. 2014) due to uncertainties in the models of

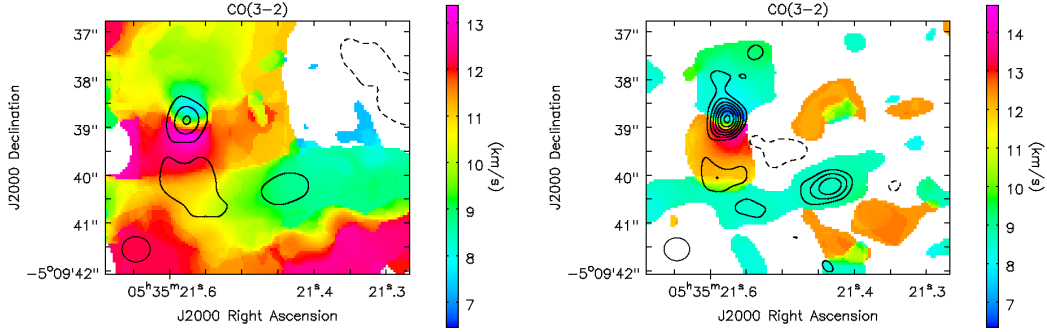


Figure 3.2: Integrated emission maps of the CO(3–2) transition including all baselines (left) and excluding all baselines shorter than $70k\lambda$ (right). Black contours are integrated line emission at $\pm 3, 5, 7 \dots 15\sigma$ where 1σ is 132 and 47 mJy beam $^{-1}$ km s $^{-1}$ respectively. Negative contours are dashed. Colors show the intensity-weighted velocity (LSRK). The beam is shown in the bottom left corner. The beam diameter is 0.5 arcsec corresponding to 200 AU at this distance.

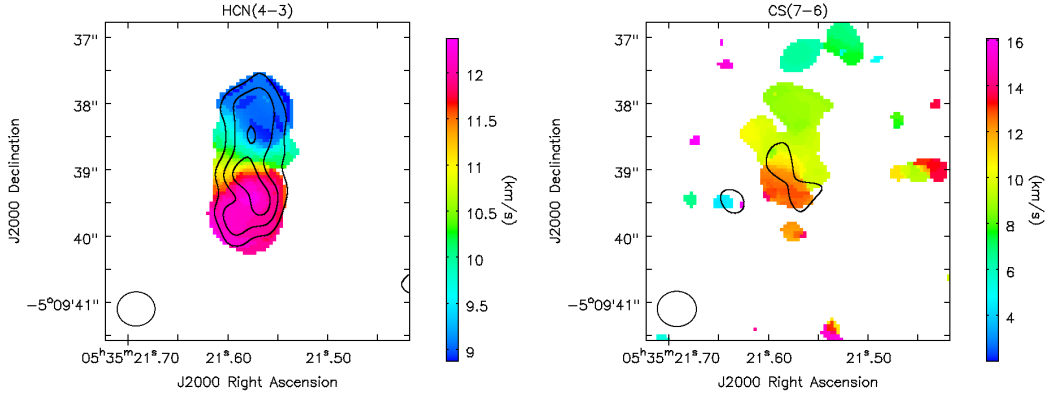


Figure 3.3: Integrated emission maps of the HCN(4–3) (left) and CS(7–6) (right) transitions. Black contours are integrated line emission at 3, 5, and 7σ where 1σ is 23 and 21 mJy beam $^{-1}$ km s $^{-1}$ respectively. Colors show the intensity-weighted velocity (LSRK). The beam is shown in the bottom left corner. The beam diameter is 0.5 arcsec corresponding to 200 AU at this distance.

Table 3.1: Integrated Flux Measurements

Line	Baselines	Integrated Line Intensity (Jy km/s)
CS(7–6)	All	0.085 ± 0.007
HCN(4–3)	All	0.84 ± 0.03
HCO ⁺ (4–3)	All	1.8 ± 0.1
HCO ⁺ (4–3)	$> 70k\lambda$	1.06 ± 0.09

Notes: Integrated line intensity was not calculated for CO(3–2) as the data were too contaminated to give a meaningful result. Uncertainties on the integrated line intensity do not include the absolute flux calibration uncertainty of the ALMA observations of $\sim 10\%$ (Mann et al. 2014).

solar system objects used as flux calibrators. Elliptical Gaussian fits to the visibilities were performed using the MIRIAD task `uvfit`. Position offset, position angle, an approximate flux, and major and minor axes were estimated from the moment maps and used as initial guesses. Channel maps for the CO(3–2) and HCO⁺(4–3) emission are shown in Figures 3.4 and 3.5 while the same maps excluding baselines shorter than $70 k\lambda$, which were used for fitting, are shown with residuals in Figures 4.4, 4.6, 4.8 and 4.9.

Assuming optically thin emission and LTE, the gas mass, M , is given by

$$M = \frac{4\pi}{h\nu_0} \frac{Fmd^2}{A_{u\ell}X_u}, \quad (3.1)$$

where ν_0 is the rest frequency of the line, F is the integrated flux in the line, m is the mass of the gas molecule, d is the distance to the source, $A_{u\ell}$ is the Einstein coefficient for the ($u-\ell$) transition and

$$X_u = \frac{N_u}{N_{\text{tot}}} = (2J_u + 1) \frac{\exp[-B_0 J_u (J_u + 1) hc/kT_{\text{ex}}]}{kT_{\text{ex}}/hcB_0}. \quad (3.2)$$

Table 3.2: Gaussian Fits to Visibilities

Line	Baselines	Peak R.A. +5:35:21.5	Peak Dec. -5:09:42.0	Maj, Min, P.A. (AU, AU, deg)	Inclination (deg)
CO(3–2)	> 70k λ	1.19 ± 0.01	3.18 ± 0.03	790 ± 30, 260 ± 10, -8 ± 1	70.78 ± 0.02
HCN(4–3)	All	1.15 ± 0.02	3.08 ± 0.04	850 ± 40, 230 ± 20, -4 ± 2	74.30 ± 0.03
HCO ⁺ (4–3)	All	1.14 ± 0.01	3.19 ± 0.02	520 ± 20, 240 ± 10, -5 ± 2	62.51 ± 0.03
HCO ⁺ (4–3)	> 70k λ	1.14 ± 0.01	3.17 ± 0.02	540 ± 20, 200 ± 20, -3 ± 2	68.26 ± 0.04

Notes: Peak position is given as offset in arcsec from primary beam center. Maj, Min, and P.A. refer to the major and minor axis and position angle of the elliptical best fit Gaussian. Position angle is defined as the rotation East of North of the blue-shifted side of the disk major axis. No results are given for CO(3–2) data containing all baselines, as the data were too contaminated to give a meaningful result, and CS(7–6) emission, as the line was only detected at the 3 σ level and showed no structure.

In Equation 3.2, J_u refers to the quantum number of the upper level, B_0 is the rotational constant (in units of hc), and T_{ex} is the excitation temperature. Equation 3.1 is the mass of the gas species in question, so it must be scaled by the fractional abundance to obtain a total gas mass. As such, our calculated mass is dependent on the fractional abundance of HCO⁺. We calculate a total disk mass of $0.20 \pm 0.02 M_{\odot}$ ($210 \pm 20 M_{\text{Jupiter}}$). This calculation uses the best fit mid-plane temperature at the radius of our resolution as the excitation temperature (see Equation 4.2 for the temperature structure and Table 4.3 for the best fit parameters). This corresponds to a temperature of 27 K, well within the range of characteristic temperatures presented by Andrews & Williams (2005), determined by fitting SED’s of disks in Taurus. We also used a HCO⁺ fractional abundance of 10^{-10} . Due to uncertainties in the abundance of HCO⁺ relative to H₂, complicated by its vertical structure (see section 5.4), the uncertainty in this measurement is likely much larger than stated above.

Clear asymmetry in the spectral extent of the lines can be seen with the blue-

shifted side showing 3σ emission 2.6 and 2.1 km/s further from systemic velocity than the red-shifted side in CO and HCO⁺, respectively. A possible source of this asymmetry can be seen in the HCO⁺ emission, where there is a distinct unresolved 47 ± 6 mJy/beam peak 0.11 ± 0.03 arcsec to the north-east of the star around -6 km/s relative to systemic velocity. This feature is particularly evident toward the bottom of the position-velocity diagram for the HCO⁺⁽⁴⁻³⁾ emission, shown in Figure 3.6. We discuss possibilities for the nature of the feature in Section 5.6. A position-velocity diagram for HCO⁺⁽⁴⁻³⁾ is shown in Figure 3.6. This diagram shows the position, as a function of velocity, of emission from a cut along the major axis of the disk. The emission matches a Keplerian velocity profile of a central star slightly more massive than $2 M_{\odot}$. There is some asymmetry in the shape of the red/blue-shifted sides of the line near systemic velocity. These channels show significant cloud contamination in CO(3-2), with the disk seen in absorption. This contamination may also be present in HCO⁺, though below the noise threshold, and may be causing this asymmetry.

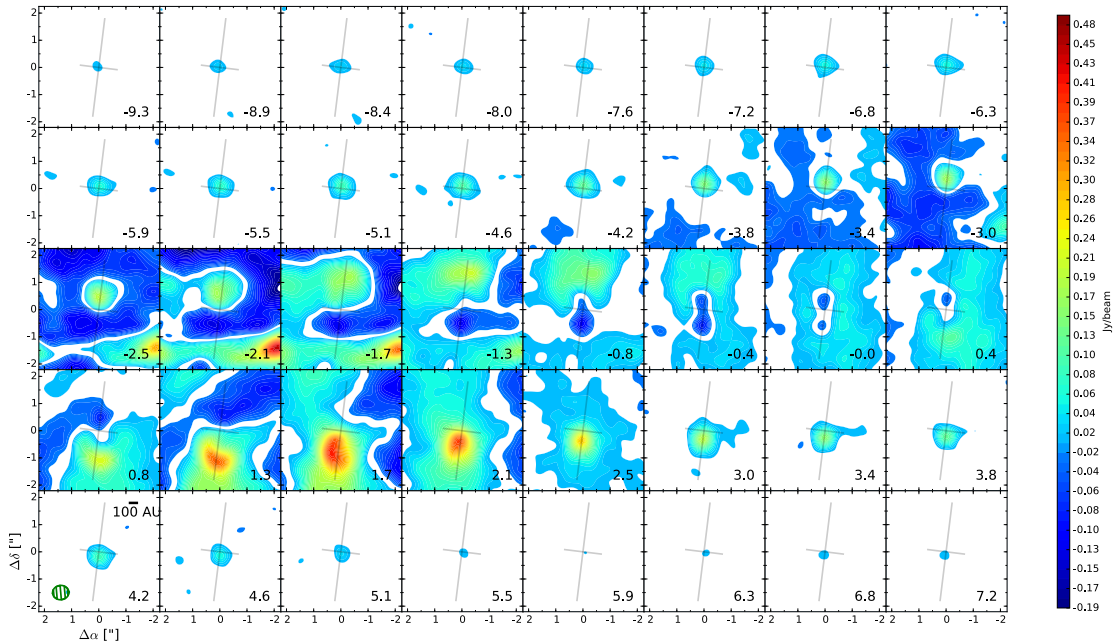


Figure 3.4: Naturally weighted channel maps of CO(3–2) emission. Colors start at $\pm 3\sigma$ with increments of 2σ up to -35σ and 90σ where 1σ is 5.47 mJy/beam. ΔV from systemic velocity (10.67 km/s LSRK) is given in the lower right corner. Synthesized beam is shown in the bottom left corner along with a 100 AU scale bar. The grey cross is centered on the star position and shows the position angle of the disk and maj/min axis ratio.

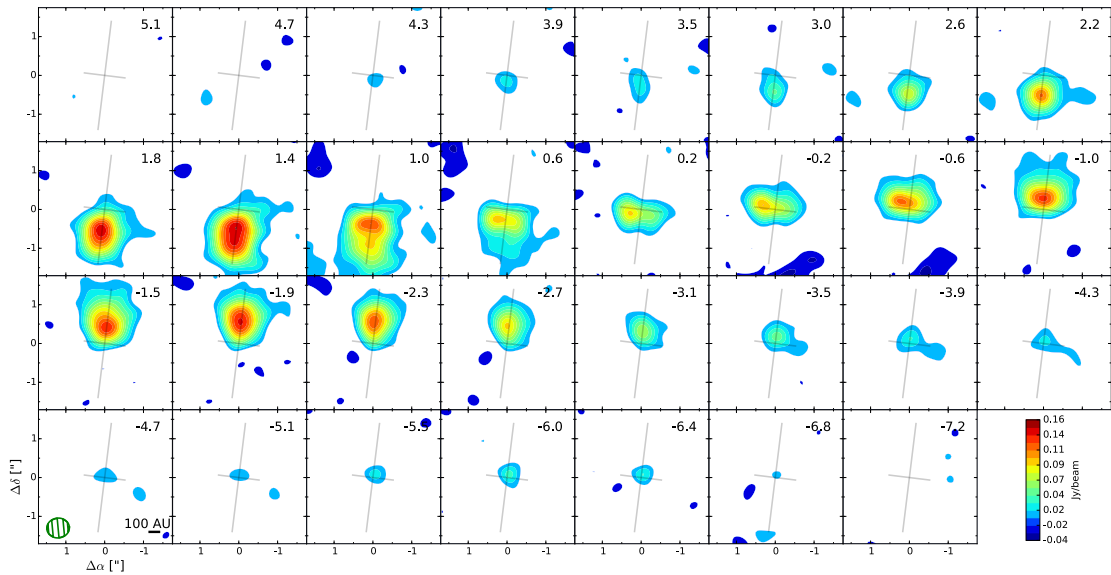


Figure 3.5: Naturally weighted channel maps of $\text{HCO}^+(4-3)$ emission. Colors start at $\pm 3\sigma$ with increments of 2σ up to -5σ and 29σ where 1σ is 5.9 mJy/beam. ΔV from systemic velocity (10.67 km/s LSRK) is given in the upper right corner. Synthesized beam is shown in the bottom left corner along with a 100 AU scale bar. The grey cross is centered on the star position and shows the position angle of the disk and maj/min axis ratio.

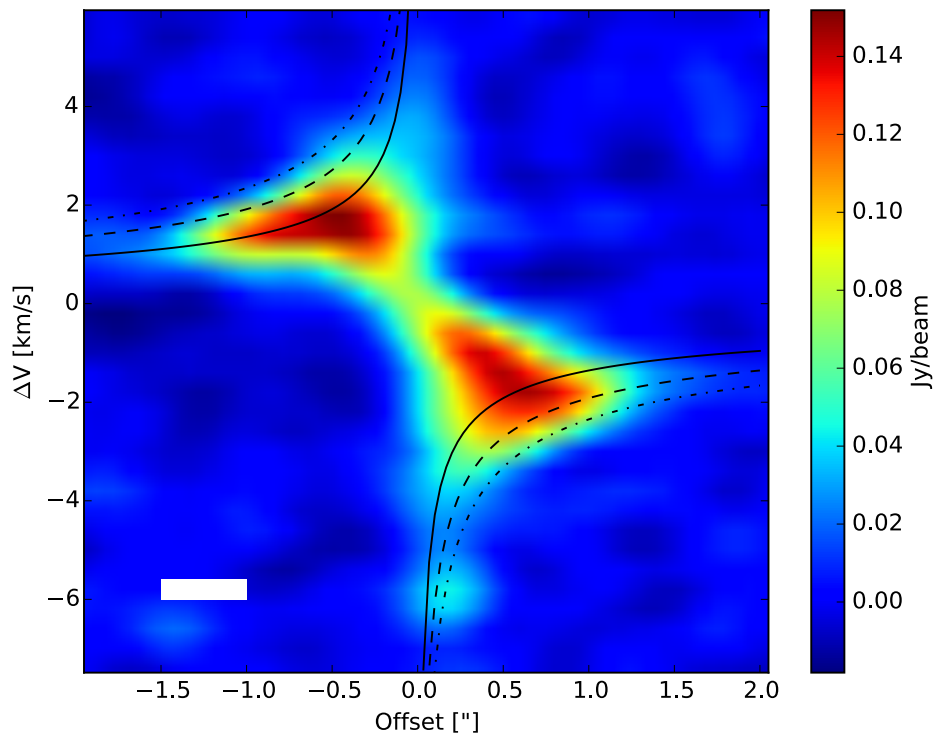


Figure 3.6: Position-velocity diagram along the disk major axis (shown in Figure 3.5) of the $\text{HCO}^+(4-3)$ emission. Solid, dashed, and dot-dashed curves are Keplerian velocity profiles for stellar masses of 1, 2, and $3 M_\odot$ respectively at an inclination of 68° , and systemic velocity of 10.67 km/s LSRK . The spatial and velocity resolution of 0.5 arcsec and 0.41 km/s are indicated by the white box in the lower left corner.

Chapter 4

Modeling

Spatially and spectrally resolved observations of gas emission allow us to determine fundamental characteristics of the disk-star system. First, the spatial structure of the emission is determined by the temperature and density profile of the disk. We can thus define this structure, perform radiative transfer, and generate a model image to compare to the data. Second, since we are looking at line emission, we can use spectrally resolved observations, and the information about the velocity field of the disk they contain, to probe both the mass of the central star and inclination of the disk (assuming Keplerian orbits). With high enough spectral resolution, which we do not have in this case, we can even determine the about of turbulence of the disk. First we must build a model of the gas emission, described in Section 4.1, which we will then fit to the data. The procedure used to fit the plentitude of input parameters to the data is recounted in Section 4.3, while the statistical fitting method is detailed in Section 4.2. Section 4.5 describes an extension of the model outlined in Section 4.1, which generates an elliptical disk.

4.1 Gas Model

The gas model used in this work was originally written in IDL by Rosenfeld et al. (2012a, 2013). It was then translated into python by Flaherty et al. (in prep). It is a ray tracing radiative transfer code based on a few simplifying assumptions. The first, and most significant assumption is that the disk is in local

thermodynamic equilibrium (LTE). While the assumption of LTE is not always valid in protoplanetary disks, Pavlyuchenkov et al. (2007) showed that it is appropriate for CO. We investigate the robustness of the LTE assumption for the HCO⁺(4–3) line in Section 4.4. The computational efficiency of the assumption enables the use of the Markov Chain Monte Carlo (MCMC) technique which can be used to robustly characterize the parameter space including the posterior distribution on each parameter taking into account degeneracies between parameters. The second assumption is that the gas kinematics are described by a Keplerian velocity field with no vertical component,

$$v_\phi(r) = \sqrt{\frac{GM_*}{r}}; \quad v_r = v_z = 0. \quad (4.1)$$

This is a valid assumption as long as $M_{disk} \ll M_*$, which is consistent with constraints from continuum observations.

We adopt the parameterization of disk temperature structure from Dartois et al. (2003) which was derived as an analytical approximation to the output of 2-D radiative transfer calculations for an optically thick dust disk. The radial temperature profile is a simple power law indexed by q , while the vertical profile is somewhat more complicated and is characterized by a height z_q . The global temperature profile is then

$$T_{\text{gas}}(r, z) = \begin{cases} T_a + (T_m - T_a) \left[\cos \frac{\pi z}{2z_q} \right]^{2\delta} & \text{if } z < z_q \\ T_a & \text{if } z \geq z_q \end{cases} \quad (4.2)$$

where the atmospheric temperature $T_a = T_{atm,150}(r/150\text{AU})^{-q}$ and the mid-plane temperature $T_m = T_{mid,150}(r/150\text{AU})^{-q}$. The height of the disk, controlled by z_q is assumed to have a radial distribution described by a power law, $z_q =$

$z_{q,150}(r/150\text{AU})^{1.3}$. Here we set δ to 1, though it can take on values $\delta \approx 1 - 2$.

The density structure is based on work by Lynden-Bell & Pringle (1974) and Hartmann et al. (1998) modeling a thin viscous accretion disk. The gas surface density profile is a tapered power law,

$$\Sigma_{\text{gas}}(r) = \frac{M_{\text{gas}}(2 - \gamma)}{2\pi R_c^2} \left(\frac{r}{R_c}\right)^{-\gamma} \exp\left[-\left(\frac{r}{R_c}\right)^{2-\gamma}\right] \quad (4.3)$$

where R_c sets the radial size of the gas disk, γ is a power law index, and M_{gas} is the total gas mass. This tapered power law structure is more physically plausible for an isolated disk than a truncated power law (a strict outer radius instead of an exponential tail). Hughes et al. (2008b) also showed that this structure resolves apparent discrepancies in the extent of continuum versus gas emission as it allows gas emission to persist at larger radii when the continuum emission has fallen off below the noise level.

We assume that $M_{\text{gas}} = M_{\text{disk}}$ as the dust makes up $\sim 1\%$ of the disk mass. The density structure $\rho(r, z)$ is then calculated by solving the equation of hydrostatic equilibrium,

$$-\frac{\partial \ln \rho_{\text{gas}}}{\partial z} = \frac{\partial \ln T_{\text{gas}}}{\partial z} + \frac{1}{c_s^2} \left[\frac{GM_*z}{(r^2 + z^2)^{3/2}} \right], \quad (4.4)$$

by integration, where

$$c_s^2 = \frac{k_B T_{\text{gas}}}{\mu m_h} \quad (4.5)$$

is the sound speed and μm_h is the mean molecular weight. In the mid-plane of the disk the temperatures are cold enough for CO to freeze out onto dust grains. We apply this freezeout by dropping the density by a factor of 10^{-18} wherever the temperature is less than 19K. The upper surface is governed by photodissociation by stellar radiation. We thus drop the density wherever the hydrogen column

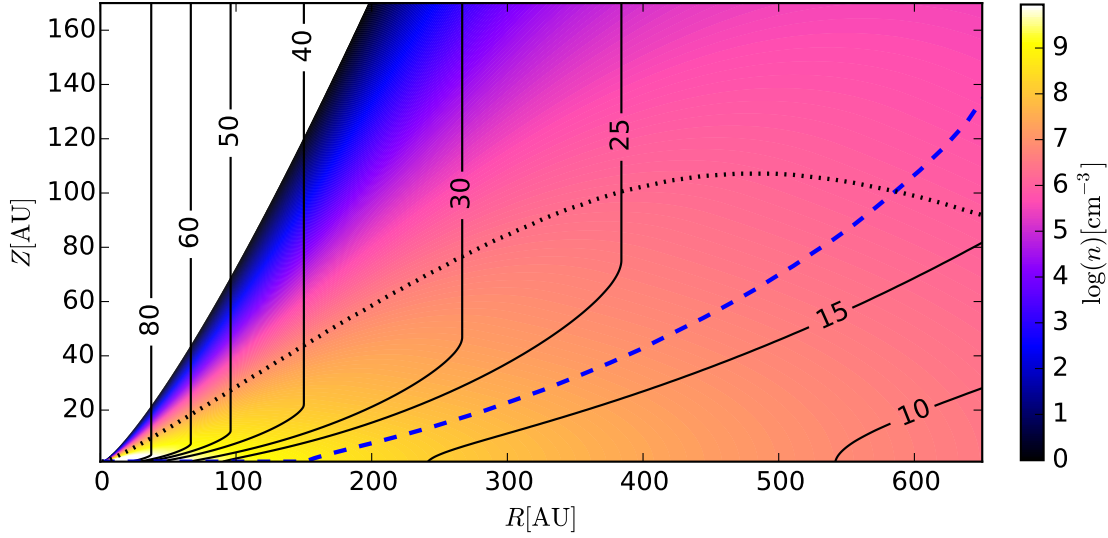


Figure 4.1: A typical density and temperature structure as described in Section 4.1. Number density of H_2 gas is shown in color while contours show temperature in units of K. The blue dashed line shows the height at which CO freezes out ($T=19$ K) and the black dotted line shows the height at which CO is photoevaporated. CO only exists in the “warm molecular layer” between these two surfaces.

density from the surface of the disk is less than $1.3 \times 10^{21} \text{ cm}^{-2}$. The temperature and column density values were determined by fits to observations of HD 163296 by Qi et al. (2011), while other values have been used elsewhere (e.g. 5×10^{20} and $9 \times 10^{20} \text{ cm}^{-2}$ for an vertically isothermal and structured disk respectively, Rosenfeld et al. 2013). A typical temperature and density structure is shown in Figure 4.1.

We then calculate the velocity profile according to equation 4.1 with a small correction for pressure and height (while still restricting orbits to be parallel to the plane of the disk). Since a gradient in pressure results in a force we must correct for this according to

$$\frac{v_\phi^2}{r} = \frac{GM_*r}{(r^2 + z^2)^{3/2}} + \frac{1}{\rho_{\text{gas}}} \frac{\partial P_{\text{gas}}}{\partial r}. \quad (4.6)$$

At this point, the physical structure (temperature, density and velocity) of the disk is completely determined and we are ready to begin calculating radiative transfer to generate an image. We calculate the specific intensity by integrating the equation of radiative transfer,

$$I_\nu = \int_0^\infty K_\nu(s) S_\nu(s) e^{-\tau_\nu(s)} ds, \quad (4.7)$$

where $K_\nu(s)$ is the absorption coefficient, $S_\nu(s)$ is the source function, and $\tau_\nu(s)$ is the optical depth. The source function in this case is $B_\nu(T)$, the Planck function. The optical depth along a line of sight s is defined by

$$\tau_\nu(s) = \int_0^s K_\nu(s') ds'. \quad (4.8)$$

We then calculate the absorption coefficient $K_\nu(s) = n_\ell(s)\sigma_\nu(s)$ from the level populations, $n_\ell(s)$, and absorption cross section, $\sigma_\nu(s)$. The level populations are determined by the Boltzmann equation,

$$n_\ell(s) = \frac{X_{\text{gas}}\rho(s)}{\mu m_H} \cdot \frac{g_\ell}{Z} \exp\left(-\frac{E_\ell}{kT(s)}\right), \quad (4.9)$$

where E_ℓ is the transition energy, $g_\ell = 2\ell + 1$ is the statistical weight, Z is the partition function, and X_{gas} is the fractional abundance (relative to H₂) of the gas in question (CO or HCO⁺) which is assumed to be homogeneous. The absorption cross section,

$$\sigma_\nu(s) = \phi_\nu(s) \cdot \sigma_0(1 - e^{-h\nu/kT(s)}), \quad (4.10)$$

is determined by the integrated cross section,

$$\sigma_0 = \frac{h\nu}{4\pi} \cdot \frac{g_{\ell+1}}{g_\ell} B_{21} = \frac{c^2}{8\pi\nu^2} \cdot \frac{g_{\ell+1}}{g_\ell} A_{21}, \quad (4.11)$$

and the line profile $\phi_\nu(s)$. The line profile is determined by three types of broadening: rotational, thermal, and turbulent. To account for rotational broadening, we must first consider the geometry of the disk, specifically its inclination i (using the convention that $i = 0^\circ, 90^\circ$ corresponds to a face and edge on disk respectively). The velocity field given by Equation 4.6 must then be projected along the line of sight $v_s = v_\phi(r) \cos \phi \sin i$. For each observed frequency ν we can calculate a velocity $v_\nu = c(\nu - \nu_0)/\nu_0$ from the rest frequency ν_0 of the line in question. The line profile is then

$$\phi_\nu(s) = \frac{c}{\sqrt{\pi}\nu_0\Delta v} \exp \left[- \left(\frac{v_\nu - v_s}{\Delta v} \right)^2 \right]. \quad (4.12)$$

The effective line width due to thermal and turbulent broadening is given by

$$\Delta v = \sqrt{\frac{2kT(s)}{m_{\text{gas}}} + v_{\text{turb}}}, \quad (4.13)$$

where m_{gas} is the mean molecular weight of the gas species in question and v_{turb} is the turbulence speed.

We then Doppler shift the entire image to account for the systemic velocity, v_{sys} , and scale, shift, and rotate the image to account for the distance to the source d , position offset from the center of the image $\Delta\alpha$ and $\Delta\delta$, and position angle PA , defined as the rotation E of N of the blue-shifted side of the disk major axis.

We thus have a plethora of parameters which can be tuned to best fit the data.

Table 4.1: Model parameters

X_{gas}	gas fraction	R_c	critical density radius
M_{disk}	disk gas mass	γ	radial density power law
M_*	mass of star	q	radial temperature power law
v_{sys}	systemic velocity	$z_{q,150}$	disk height at 150 AU
v_{turb}	turbulence velocity	$T_{\text{mid},150}$	mid-plane temperature at 150 AU
d	distance	$T_{\text{atm},150}$	atmospheric temperature at 150 AU
i	inclination	$\Delta\alpha$	disk offset in RA from center of image
PA	position angle	$\Delta\delta$	disk offset in Dec from center of image

These parameters are summarized in Table 4.1. Given a set of input parameters, the model will generate an image with a specified spatial and spectral resolution. The spectral resolution is the same as our data and the spatial resolution is $\sim 1/10$ the size of the synthesized beam. This resolution is high enough to avoid sampling artifacts when we simulate interferometric observations of this image. We first Hanning smooth the image. This reduces the ringing in the frequency domain caused by Fourier transforming sharp features. We then simulate observations using the MIRIAD task `uvmodel` with `options=replace` and our ALMA observations as the visibility data set. The `uvmodel` task calculates the Fourier transform of the image, then samples it using the uv tracks of our observations. This creates a visibility data set of the model if it were observed with the same exact array configuration. We then calculate a χ^2 statistic by comparing the data and sampled model in the visibility domain. Using the visibilities to calculate the χ^2 statistic, rather than the images, results in a χ^2 statistic which is not affected by artifacts generated during the imaging process.

4.2 MCMC Methods

We then fit our model to the data using a Markov Chain Monte Carlo (MCMC) algorithm using an affine invariant sampler. MCMC algorithms are based on Bayesian inference, and thus allow the user to probe the posterior probability distribution. In other words, they not only find the set of best fit parameters, but also allow us to characterize that set of parameters with error bars. They work by statistically sampling χ^2 values in n -dimensional parameter space. This is accomplished by using one or more “walkers”, or points in parameter space, which move through parameter space according to a specific set of rules, discussed below. The “walkers” then generate a chain of steps (Markov chain) which can be statistically analyzed to probe the posterior distribution (the statistical distribution of best fit parameters).

A move is made by first proposing a test state. In the simplest case (the Metropolis-Hastings algorithm with a Gibbs sampler) this is chosen by changing *one* parameter from a Gaussian distribution centered at the current value of that parameter with a tunable width. The width must be tuned such that enough moves are accepted to sufficiently explore parameter space, but not enough that good fits are ignored. For example if the width is too wide, a given proposed step is more likely to be rejected as it is far away from the current model. Thus parameter space is not well sampled. On the other hand, if the width is too narrow, a step is more likely to be accepted as the proposed χ^2 value will be similar to the current value. In this case, parameter space will be explored though inefficiently due to the small steps sizes. Depending on the dimensionality of the parameter space you are sampling, the acceptance fraction, $n_{\text{accept}}/n_{\text{reject}}$, should be in the 0.2–0.5 range for optimum efficiency.

A χ^2 metric is then calculated for the new test state and compared to the current state. The test state is accepted with a probability $p = \exp[(\chi_{\text{current}}^2 - \chi_{\text{test}}^2)/2]$. That is, if the test state has a smaller χ^2 value than the current state, $p > 1$ and the test state is accepted and becomes the new current state. On the other hand, if the test state has a larger χ^2 value, it may still be accepted, with a probability ($p < 1$) proportional to how much “worse” it is. This decision can be easily implemented in code by generating a random number, ξ , between 0 and 1; if $\xi < p$ then the new state is accepted, and if $\xi > p$ the new state is rejected. While powerful, this method does not sample degenerate parameter spaces well, due to the fact that it only changes one parameter at a time, so that steps through parameter space are orthogonal to each other.

Since many of our model parameters are degenerate with each other, we must use a different sampler which will allow us to sample parameter space more efficiently. We chose to use the open source `emcee` (The MCMC Hammer) package for python written by Foreman-Mackey et al. (2013) (documentation can be found at <http://dan.iel.fm/emcee/current>). This package is based on the affine invariant sampler described by Goodman & Weare (2010). It uses a group of walkers which move along lines between each other, allowing them to traverse multiple dimensions of parameter space in one move. Moves are accepted or rejected in a similar manner to the sampler described above. The package is highly customizable, extremely powerful, and parallelizable.

Starting with an initial set of models, walkers must find their way to the region of parameter space around the best fit model before they can begin statistically exploring that region. The so called “burn-in” steps must be excluded from any statistical analysis of the Markov chain. This can be seen in Figure 4.2 which shows the χ^2 values for a set of 150 walkers making 600 steps. We exclude the

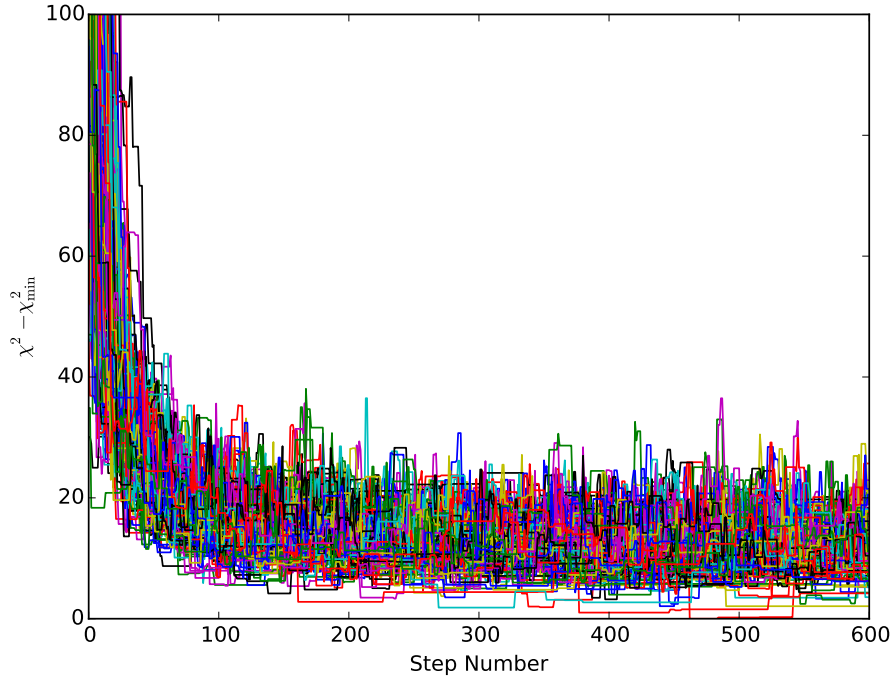


Figure 4.2: χ^2 values plotted against step number for a typical run of `emcee` using 150 walkers and 600 steps.

first ~ 250 steps from our statistical calculations. We draw the starting positions of our walkers from an n -dimensional Gaussian ball around our previous best fit model (or an educated guess for the first run). The widths in each dimension are set according to the width of the previous posterior distribution, or a reasonable width determined from the literature. The initial positions of the walkers do not affect the best fit model, only the burn in time.

Once the walkers have sufficiently explored parameter space around the best fit model, we can analyze the Markov chain they have generated in order to statistically characterize the posterior probability distribution. First, how do we know that the walkers have sufficiently explored parameter space? We look at the autocorrelation values for each parameter. We exclude the first $\gtrsim 3$ autocorrelation times for burn-in and use at least 3 more in our statistical analysis. In some cases,

individual walkers that had not burned in even after 3 autocorrelation times had to be removed. This would be obvious when plotting χ^2 values as in Figure 4.2; a few walkers would drop down from above and join the rest near the best fit model. In general, more walkers and more steps are better, until you hit performance constraints. We ran our fitting routines on Wesleyan’s High Performance Compute Cluster (HPCC). Our single-line fits took $\sim 3 - 4$ days to run while our double-line fits took ~ 8 days.

In order to visualize the Markov chains, `emcee` provides a tool to make triangle plots. Triangle plots show the density of tested models in each dimension of parameter space individually and compared to each other dimension. In this way we can see how well constrained each parameter is, and if there any degeneracies between parameters. Degeneracies can be seen in Triangle plots specifically in the panes which show the correlation between two parameters. If the two parameters are not degenerate the overall density should be a circular Gaussian. On the other hand, if two parameters are degenerate with each other, the density will have an angled and elongated shape.

4.3 Fitting Procedure

Once we have defined our model we can now begin the fitting procedure. All fits were performed on data that excluded baselines shorter than $70k\lambda$ to minimize cloud contamination (see Section 3.1 for a discussion of contamination). First, we performed a simple grid search for the x-y position offset from the center of the image and the systemic velocity, using a typical set of parameters along with an inclination and position angle determined from the images and previous observations. We used only the HCO⁺(4-3) line for these preliminary fits, since

that line has the least contamination. We took care to exclude channels with the excess high velocity emission discussed in Chapter 3 when performing all fits, but most importantly when fitting the systemic velocity (see Section 4.5 for a discussion of this importance). Channels with velocities less than or equal to -5.1 km/s (relative to systemic velocity) were excluded from fits to the HCO⁺(4–3) data. These fits gave us a systemic velocity of 10.7 ± 0.1 km/s and a $\Delta\alpha$ and $\Delta\delta$ of 3.13 ± 0.02 and 1.17 ± 0.02 arcsec, respectively (the center of the primary beam is 5h 35m 21.5s RA, $-5^{\circ}09'42.0''$ Dec). The grid searches had step sizes of 0.01 km/s and 0.01 arcsec.

4.3.1 HCO⁺(4–3) Fit

We then focused on fitting (using the previously discussed MCMC method) the rest of the parameters using the HCO⁺(4–3) line. Since we were only modeling one line, we could not constrain the vertical temperature structure and thus fixed $T_{\text{mid},150}$ and $z_{q,150}$ at 19 K and 29 AU respectively. The mid-plane temperature was chosen to reproduce the midplane temperature structure and “CO snow line” observed by Qi et al. (2011). While these observations were of a different disk in a different environment, the measurement provides a starting point for our fits. $z_{q,150}$ was chosen to be approximately twice the scale height, following Rosenfeld et al. (2013). Since HCO⁺(4–3) is optically thin, the temperature and density structure are degenerate and we fixed γ at -1 , a typical value for disks in Ophiuchus (Andrews et al. 2009, 2010). We also fixed X_{HCO^+} at 10^{-10} . This value was chosen for a few reasons. While it is on the low end of typical ISM and disk HCO⁺ abundances ($10^{-9} \pm 1$ dex, Aikawa & Herbst 1999; Fogel et al. 2011), it gave the best fit (determined by inspecting the residuals) of values in that range. We are

also using a constant abundance throughout the disk which is a simplification of the actual structure discussed in more detail in Section 5.3. Our observations do not have high enough spectral resolution to constrain the turbulent linewidth so we fixed v_{turb} at 1% of the sound speed.

We also placed a prior on the disk mass by adding a term to the log likelihood function (normally just $-\chi^2/2$). This extra term was of the form

$$-\ln \left(\frac{1}{\sigma \sqrt{2\pi}} e^{-(p-\mu)^2/2\sigma^2} \right) \quad (4.14)$$

where p corresponds to $\log M_{\text{disk}}$ of the model, μ is $\log 0.044$ corresponding to the previously measured disk mass (Mann et al. 2014, measured from continuum observations), and $\sigma = 1$ corresponding to a width of 1 order of magnitude. This was done to constrain the disk mass near the previously measured value but still allow the parameter to vary.

A triangle plot, showing the posterior distributions of the individual line fit, is shown in Figure 4.3. Best fit and median values with 1σ uncertainties are given in Table 4.2. All parameters seem to be well constrained with noticeable degeneracies between parameters affecting the temperature structure (q and $T_{\text{atm},150}$) and density structure (M_{disk} and R_c). Noticeably absent is the expected degeneracy between inclination, i , and stellar mass, M_* . The inclination of the disk affects the projection of the Keplerian velocity on to the line of sight which effects the measured mass. For example, decreasing the inclination will result in a slower velocity field which is fit by a smaller stellar mass. The absence of the expected degeneracy is due to the fact that the spatially resolved observations place tight constraints on the inclination (assuming a circular orbit)).

Channel maps showing residuals from the best fit model, compared to the

Table 4.2: Best Fit Parameters to Individual Lines

Parameter	HCO ⁺ (best)	HCO ⁺ (median)	CO (best)	CO (median)
q	-0.02	$0.07^{+0.07}_{-0.06}$	-0.30	-0.36 ± 0.09
M_{disk} (M_{\odot})	0.10	$0.05^{+0.02}_{-0.01}$	0.02	$0.06^{+0.27}_{-0.04}$
R_c (AU)	210	200 ± 20	77	140^{+820}_{-80}
M_* (M_{\odot})	2.06	2.08 ± 0.05	2.6	$2.5^{+0.1}_{-0.2}$
$z_{q,150}$ (AU)	[29]	[29]	[29]	[29]
$T_{\text{mid},150}$ (K)	[19]	[19]	[19]	[19]
$T_{\text{atm},150}$ (K)	22	25^{+4}_{-3}	41	41^{+5}_{-3}
$\log X_{\text{gas}}$	[-10]	[-10]	[-4]	[-4]
i (deg)	66.7	67.5 ± 0.8	65	65 ± 3
PA (deg)	-7.3	-6.9 ± 0.8	1	3 ± 3

Notes: Parameters in square brackets were fixed. In all fits d was fixed at 400 pc, v_{turb} to $0.01c_s$, γ to -1, v_{sys} to 10.67 km/s and $\Delta\alpha$ and $\Delta\delta$ to 3.13 and 1.17 arcsec respectively. Stated uncertainties do not include the ALMA absolute flux uncertainty of $\sim 10\%$ or the distance uncertainty of 1.5%.

corresponding data, are shown in Figure 4.4. Significant residuals in high velocity blue-shifted channels are to be expected as we did not model the asymmetric emission in those channels. Elsewhere, 5σ residuals are only located in channels with significant cloud contamination in CO. It is reasonable to assume there may be some associated contamination in HCO⁺ which could be causing asymmetries in the disk emission in those channels.

4.3.2 CO(3–2) Fit

Even after excluding baselines shorter than $70k\lambda$, CO(3–2) emission was still highly contaminated in channels near the systemic velocity. Fits to the individual CO(3–2) line, only modeling uncontaminated channels, showed asymmetry between the red- and blue-shifted sides of the disk in a similar manner to the asymmetry seen in the HCO⁺(4–3) emission. In CO(3–2), this excess emission is

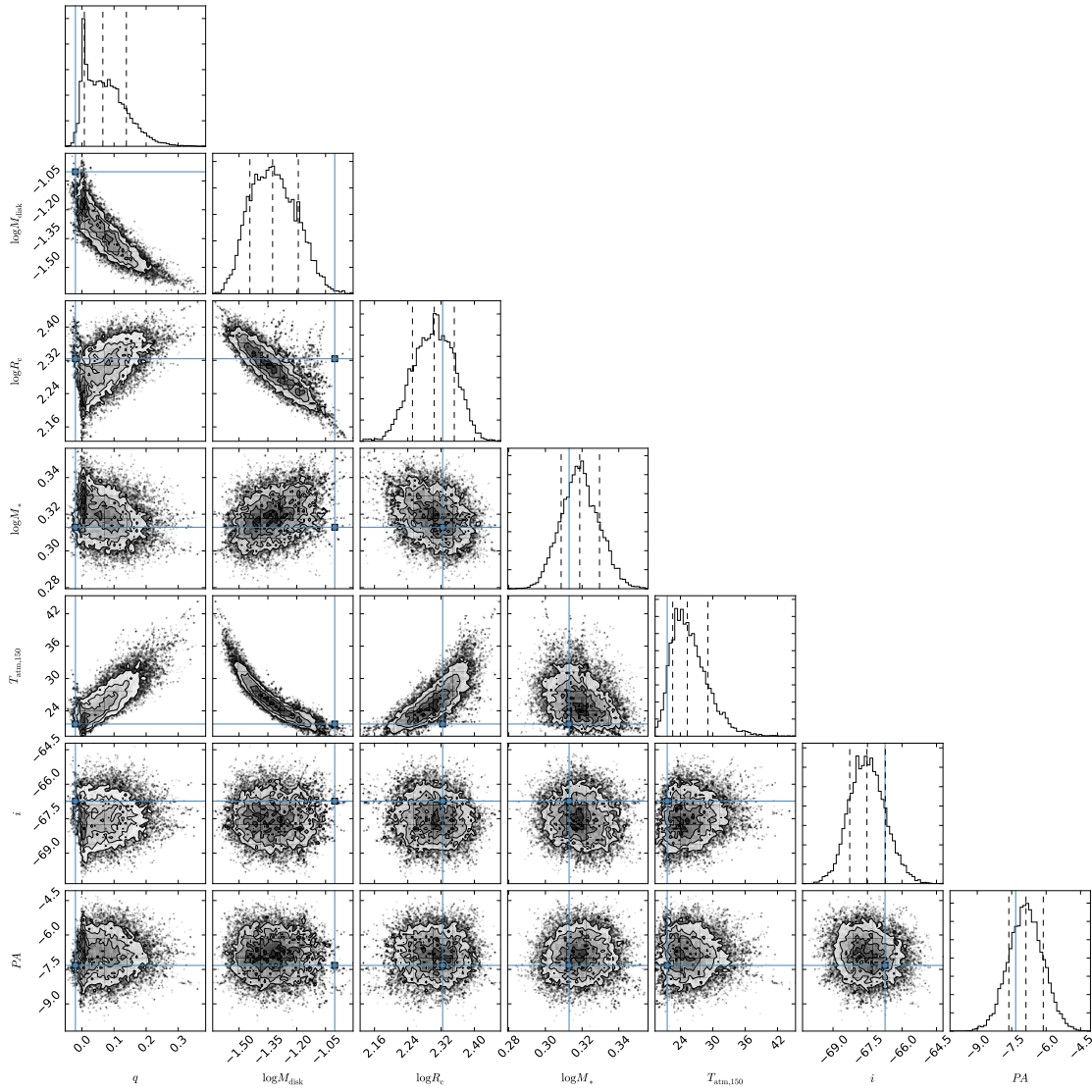


Figure 4.3: Triangle plot showing the posterior probability distributions of the 7 parameter fit to the $\text{HCO}^+(4-3)$ emission (values given in Table 4.2). Plots along the diagonal show the posterior of each parameter individually while plots below the diagonal compare a pair of parameters showing potential degeneracies. Solid blue lines show the best fit parameter values while dashed lines show the median and $\pm 1\sigma$ values.

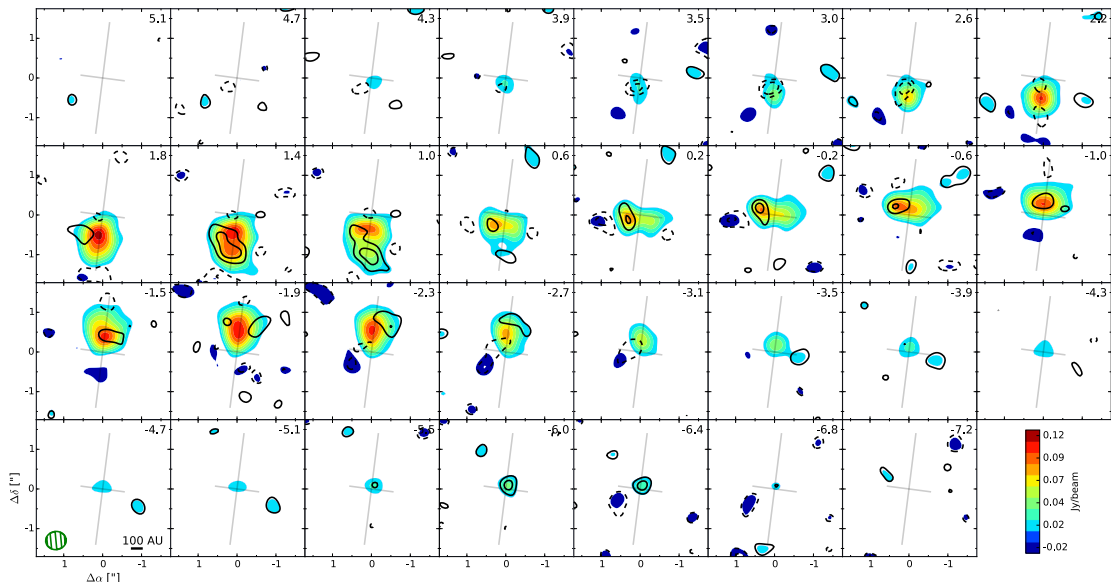


Figure 4.4: Naturally weighed channel maps of $\text{HCO}^+(4-3)$ emission excluding baselines shorter than $70k\lambda$. Colors and contours start at $\pm 3\sigma$ with increments of 2σ up to 19σ where 1σ is 6.2 mJy/beam. Dashed contours correspond to negative values. Contours are residuals from the best fit to the $\text{HCO}^+(4-3)$ line only, given in Table 4.2. ΔV from systemic velocity (+10.67 km/s LSRK) is given in the upper right corner. Channels with $\Delta V \leq 5.1$ km/s were excluded when fitting. The synthesized beam is shown in the bottom left corner along with a 100 AU scale bar. The grey cross is centered on the star position and shows the position angle of the disk and maj/min axis ratio.

only seen in the spectral extent of the blue-shifted side of the line and not as a second peak as in the HCO⁺(4–3) line. Thus when fitting CO(3–2), we excluded the entire blue-shifted side of the line along with the contaminated channels near systemic velocity. This corresponds to only modeling channels with velocities greater than and including 3.0 km/s relative to the systemic velocity.

The set of best fit parameters (q , M_{disk} , M_* , R_c , $T_{\text{atm},150}$, i , and PA) from fitting only the HCO⁺(4–3) line was used as a starting point to fit the CO(3–2) line individually. The same set of fixed parameters were used for fitting the CO(3–2) data with the exception of X_{CO} which was fixed to 10^{-4} , the accepted value for protoplanetary disks and the ISM (Aikawa & Herbst 1999; Fogel et al. 2011). We placed the same prior on the disk mass as described previously for fitting HCO⁺(4–3).

A triangle plot, showing the posterior distributions of the individual line fit, is shown in Figure 4.5. Best fit and median values with 1σ uncertainties are again given in Table 4.2. All parameters seem to be well constrained with the exception of M_{disk} and R_c . Since CO(3–2) is optically thick we would expect it to provide a lower limit on the mass which is clearly seen in the triangle plot as a sharp drop off in the posterior distribution near $0.02 M_\odot$. The outer radius is constrained mainly by the channels near systemic velocity, which we are not fitting, thus R_c is not well constrained. The inclination and position angle have much larger uncertainties than those of the fit to the HCO⁺(4–3) line for the same reason. In this fit the expected degeneracy between inclination, i , and stellar mass, M_* is seen due to the poorly constrained inclination.

Channel maps showing residuals from the best fit model, compared to the corresponding data, are shown in Figure 4.6. Significant residuals in high velocity blue-shifted channels and those near systemic velocity are to be expected as we

did not model those channels. Residuals in the channels which were modeled are minimal.

4.3.3 Combined Fit

The set of best fit parameters (q , M_{disk} , M_* , R_c , $T_{\text{atm},150}$, i , and PA) from fitting only the $\text{HCO}^+(4-3)$ line was used as a starting point to fit the $\text{HCO}^+(4-3)$ and $\text{CO}(3-2)$ lines together. With multiple lines we can constrain the vertical temperature structure so $T_{\text{mid},150}$, $z_{q,150}$ were allowed to vary. We fixed X_{CO} at 10^{-4} , the value of the ISM.

In our early two-line fits, M_{disk} was allowed to vary while X_{HCO^+} was fixed. The results were fits that seemed to converge well, but produced significant residuals. $\text{CO}(3-2)$ fit well, but $\text{HCO}^+(4-3)$ was much too bright. We thus allowed X_{HCO^+} to vary and control the relative line intensities. While this did produce better fits, the parameters were not reasonable.

The $\text{CO}(3-2)$ emission, which does not constrain the disk mass, seemed to be pulling that parameter up. This caused the HCO^+ abundance to drop in order to keep that line fitting well. The posterior distribution of X_{HCO^+} was also bimodal and showed a degeneracy with disk mass. Best fit values for X_{HCO^+} were between 10^{-11} and 10^{-10} but a second peak near 10^{-7} . The lower abundance models fit a disk mass between 0.4 and $1 M_\odot$, clearly outrageous values. The higher abundance models fit a disk mass of $0.08 M_\odot$, much closer to the mass derived by fitting $\text{HCO}^+(4-3)$ individually and the continuum mass measurement discussed earlier. Consequently, we decided to fix the disk mass while still fitting the HCO^+ abundance. This removed any influence the $\text{CO}(3-2)$ emission had on the disk mass. We placed a prior on X_{HCO^+} centered at 10^{-9} with a width of 1

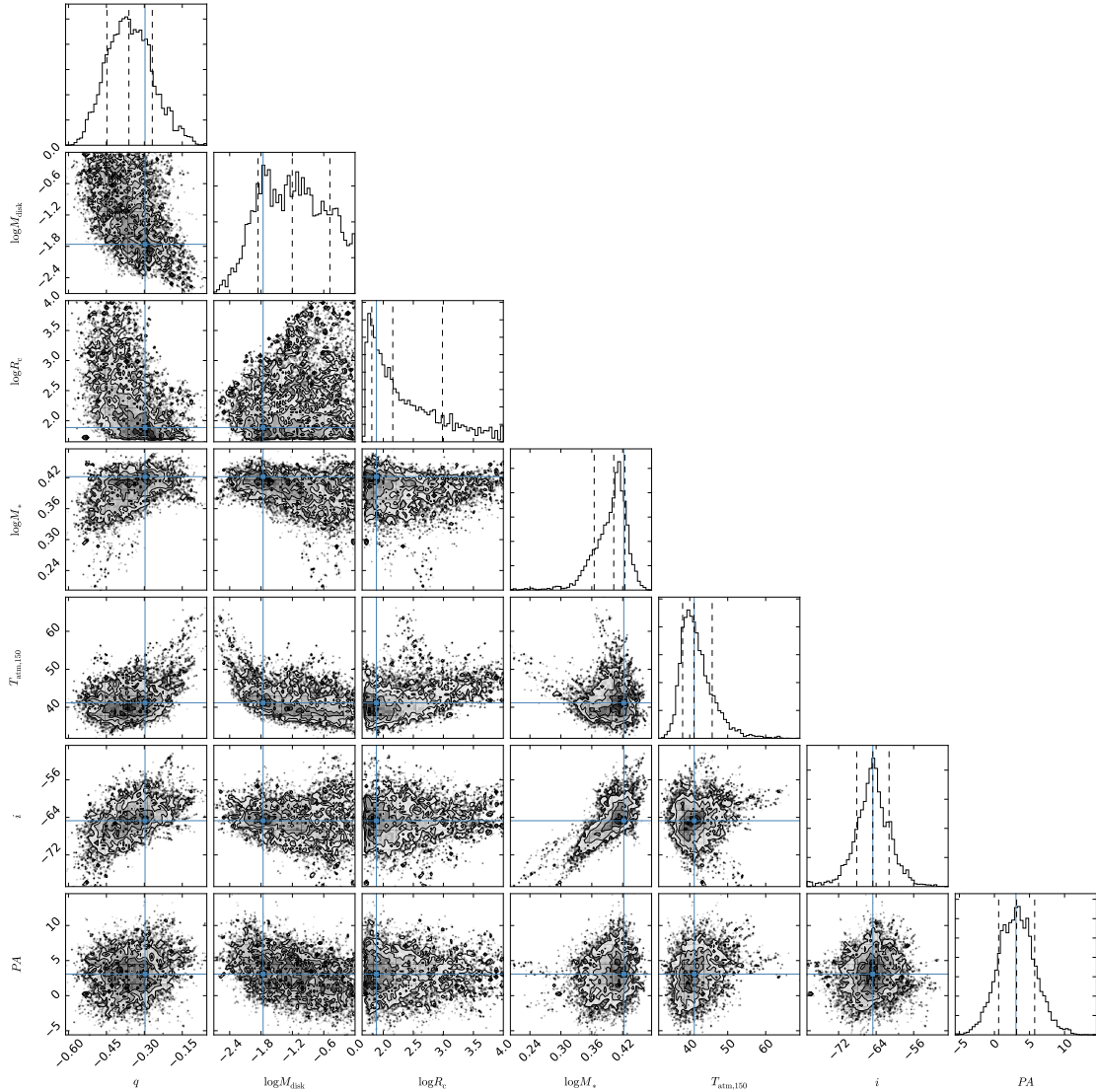


Figure 4.5: Triangle plot showing the posterior probability distributions of the 7 parameter fit to the CO(3–2) emission (values given in Table 4.2). Symbols are the same as Figure 4.3.

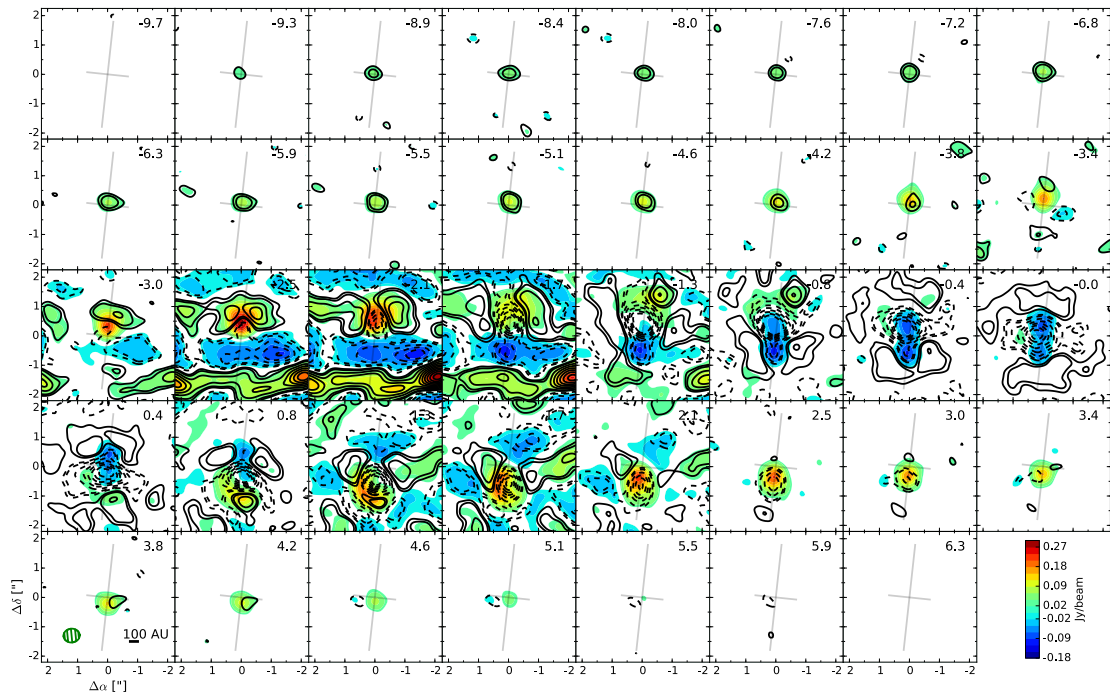


Figure 4.6: Naturally weighed channel maps of CO(3–2) emission excluding baselines shorter than $70k\lambda$. Colors and contours are at 3, 5, 10, 15...45 σ 1σ is 5.9 mJy/beam. Contours are residuals from the best fit to the CO(3–2) line only, given in Table 4.2. Symbols are the same as in Figure 4.4. Channels with $\Delta V < 3.0$ km/s were excluded when fitting.

Table 4.3: Best Fit Parameters to Both Lines

Parameter	CO & HCO ⁺ (best)	CO & HCO ⁺ (median)
q	-0.24	-0.25 ± 0.02
M_{disk} (M_{\odot})	[0.045]	[0.045]
R_c (AU)	850	1000^{+300}_{-200}
M_* (M_{\odot})	2.20	2.19 ± 0.04
$z_{q,150}$ (AU)	73	67^{+10}_{-8}
$T_{\text{mid},150}$ (K)	24.7	25.1 ± 0.8
$T_{\text{atm},150}$ (K)	86	78^{+14}_{-9}
$\log X_{\text{gas}}$	[-4], -10.04	[-4], -10.00 ± 0.06
i (deg)	67.7	$67.2^{+0.6}_{-0.8}$
PA (deg)	-6.1	$-5.5^{+0.6}_{-0.7}$

Notes: Parameters in square brackets were fixed. d was fixed at 400 pc, v_{turb} to $0.01c_s$, γ to -1, v_{sys} to 10.67 km/s and $\Delta\alpha$ and $\Delta\delta$ to 3.13 and 1.17 arcsec respectively. Stated uncertainties do not include the ALMA absolute flux uncertainty of $\sim 10\%$ or the distance uncertainty of 1.5%.

order of magnitude ($\mu = -9$, $\sigma = 1$ and $p = \log X_{\text{HCO}^+}$ in Equation 4.14) and fixed the disk mass at $0.045 M_{\odot}$. As X_{HCO^+} is degenerate with M_{disk} we chose to fix the disk mass at the continuum derived mass Mann et al. (2014); Mann & Williams (2010, 2009a) rather than the best fit value from the HCO⁺(4–3) line. This resulted in a reasonable fit with minimal residuals.

The triangle plot for the combined two-line fit is shown in Figure 4.5. Best fit and median values with 1σ uncertainties are given in Table 4.3. Significant degeneracies can be seen between q and $T_{\text{mid},150}$, $z_{q,150}$ and $T_{\text{atm},150}$, as well as R_c and X_{HCO^+} . The degeneracy between q and $T_{\text{mid},150}$ may be related to the location of the snow line (see Section 5.3). The degeneracy between $z_{q,150}$ and $T_{\text{atm},150}$ is expected in that a thicker midplane (larger $z_{q,150}$) would result in a hotter atmospheric temperature. The strong degeneracy between R_c and X_{HCO^+} shows that HCO⁺(4–3) is controlling the flux in the outer disk since we are only

fitting CO(3–2) emission from the inner disk.

Channel maps showing residuals from the best fit model, compared to the corresponding data, are shown in Figures 4.8 and 4.9. Once again, significant residuals in high velocity blue-shifted channels in both lines and channels near the systemic velocity are to be expected as we did not model those channels. Residuals from this fit are slightly more significant than from the fits to the individual lines.

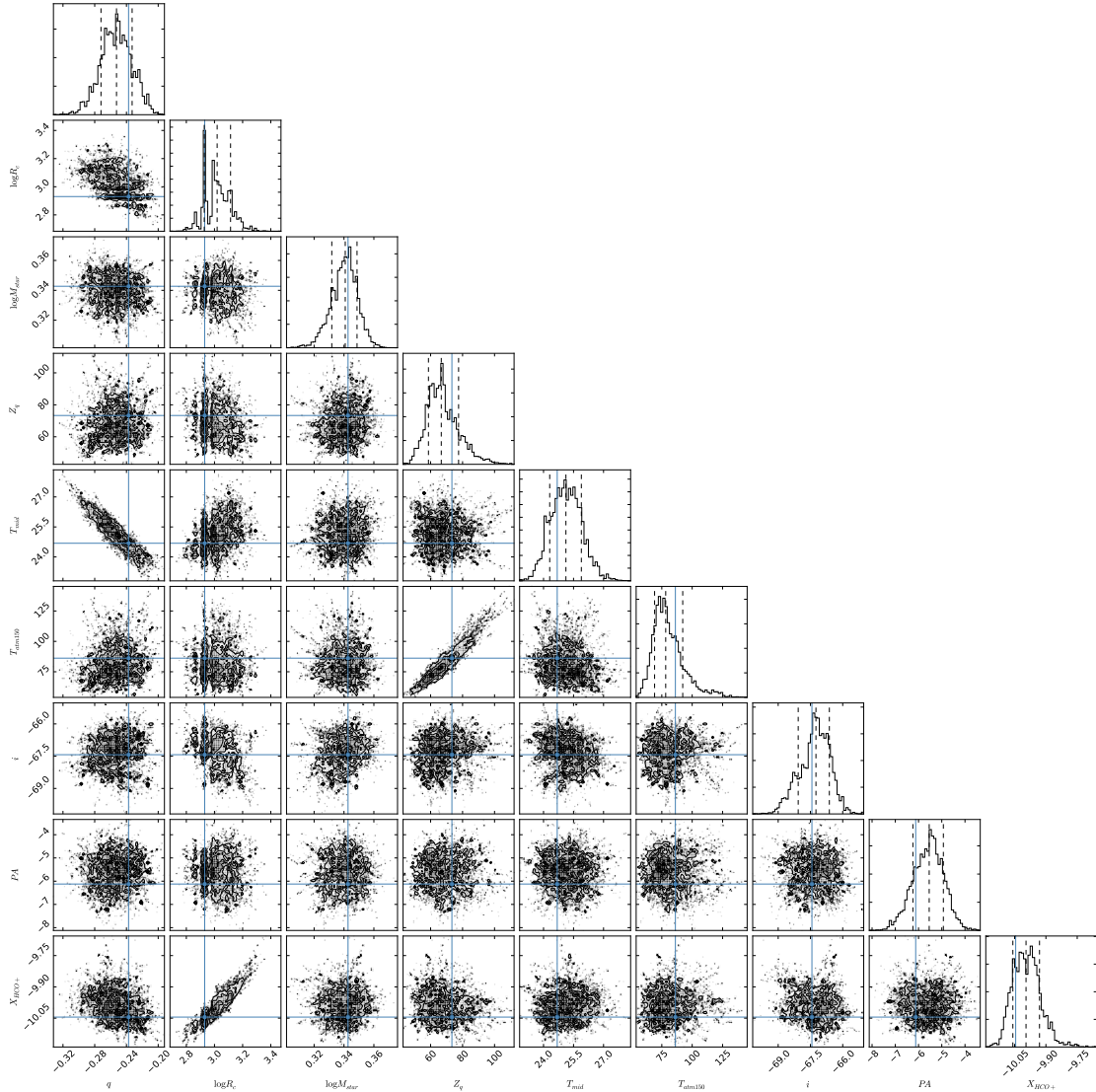


Figure 4.7: Triangle plot showing the posterior probability distributions of the 9 parameter fit to the $\text{HCO}^+(4-3)$ and $\text{CO}(3-2)$ emission (values given in Table 4.3). Symbols are the same as Figure 4.3

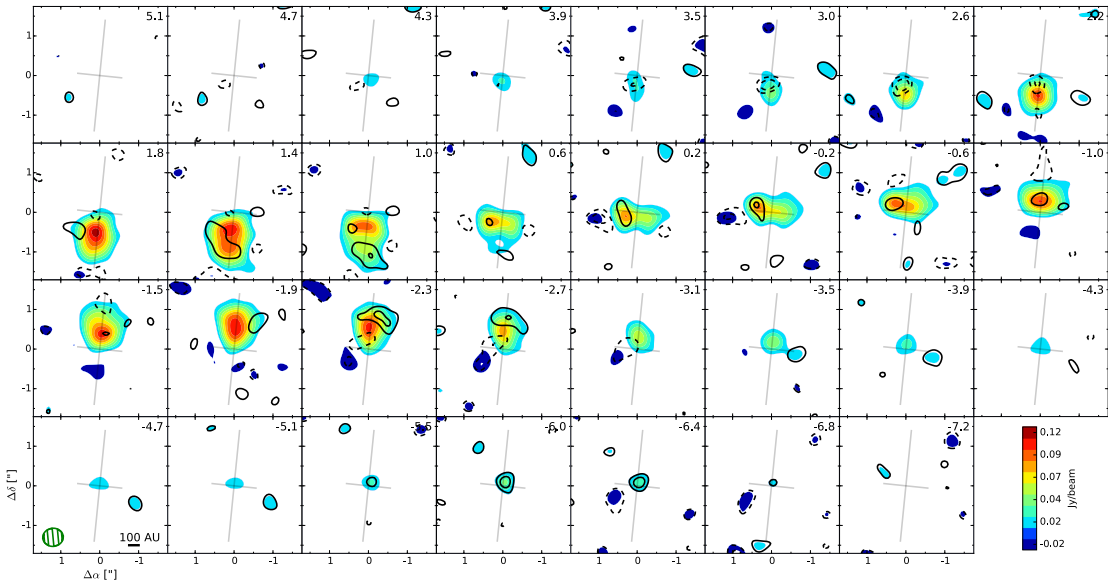


Figure 4.8: Naturally weighed channel maps of $\text{HCO}^+(4-3)$ emission excluding baselines shorter than $70k\lambda$. Colors and contours start at $\pm 3\sigma$ with increments of 2σ up to 19σ where 1σ is 6.17 mJy/beam. Contours are residuals from the best fit to the $\text{HCO}^+(4-3)$ and $\text{CO}(3-2)$ lines together, given in Table 4.3. Symbols are the same as in Figure 4.4. Channels with $\Delta V \leq 5.1$ km/s were excluded when fitting.

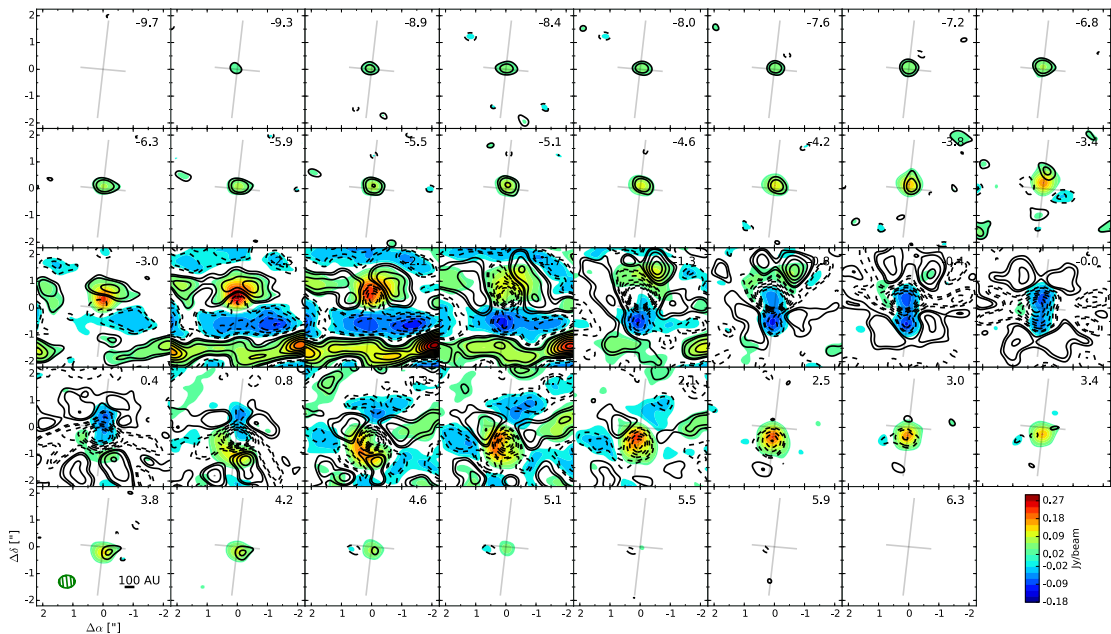


Figure 4.9: Naturally weighed channel maps of CO(3–2) emission excluding baselines shorter than $70k\lambda$. Colors and contours are at 3, 5, 10, 15...45 σ where 1σ is 5.94 mJy/beam. Contours are residuals from the best fit to the HCO⁺(4–3) and CO(3–2) lines together, given in Table 4.3. Symbols are the same as in Figure 4.4. Channels with $\Delta V < 3.0$ km/s were excluded when fitting.

4.4 Evaluation of the LTE Assumption

As discussed in Section 4.1, the assumption of local thermodynamic equilibrium (LTE) has been shown by Pavlyuchenkov et al. (2007) to be appropriate for CO, while less so for HCO⁺. We therefore investigated the differences between our LTE model and a non-LTE model using LIME (Brinch & Hogerheijde 2010). Figure 4.10 compares images of the best fit HCO⁺(4–3) model generated by the model discussed in Section 4.1 and LIME. After Hanning smoothing the full resolution images, observations were simulated using the MIRIAD task `uvmodel` using `options=replace` and our ALMA observations as the visibility data set. The sampled datasets were then compared in the visibility domain using the MIRIAD task `uvmodel` using `options=subtract` and cleaned and restored using the standard procedures in MIRIAD. Three channel maps are shown: one at the systemic velocity (line-center), one near peak intensity, and one at the high-velocity line wing.

The models differ by less than 3σ in all channels except for 2 channels which show 3σ residuals near peak intensity on both the blue and red-shifted sides of the line. Overall this shows that our assumption of LTE should not drastically affect our results and the advantage in computational efficiency and the statistical characterization it allowed outweigh the small inaccuracies in our model.

4.5 Elliptical Disk Model

As stated in Section 4.3 we were careful to exclude channels with excess high velocity emission from our fits. When performing initial fits, this was not done and our systemic velocity and position offset were thrown off. As such, residuals

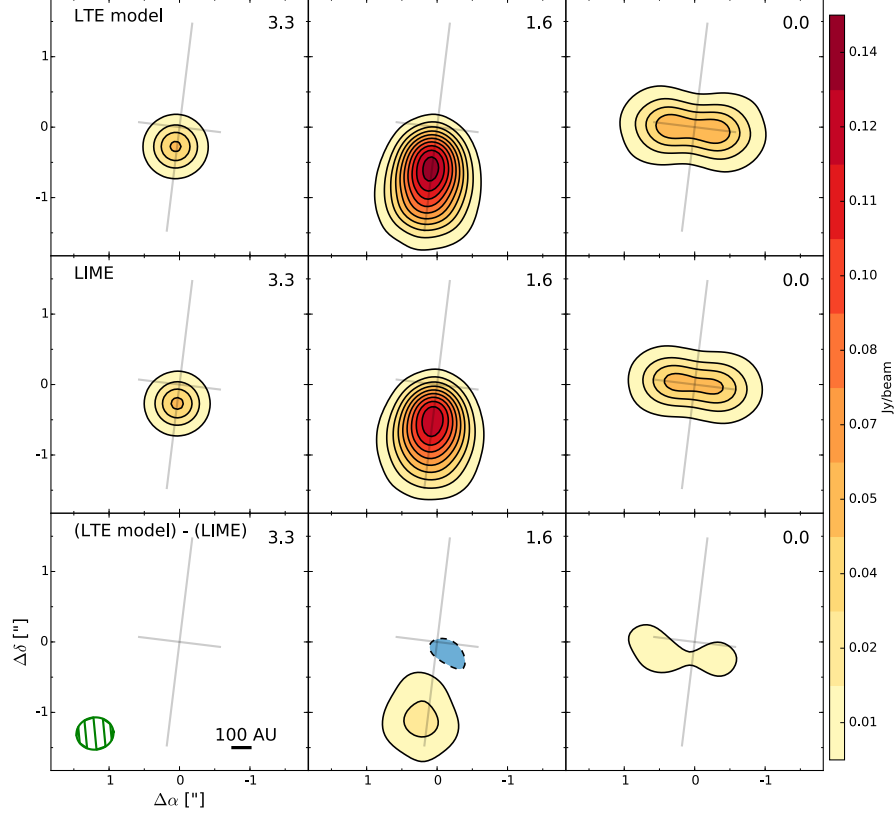


Figure 4.10: Channel maps showing simulated observations of $\text{HCO}^+(4-3)$ created using our LTE model (top), LIME (middle) and the difference (bottom). Contours start at $\pm 1\sigma$ with increments of 2σ where 1σ is 7.3 mJy/beam, the same as our $\text{HCO}^+(4-3)$ observations. ΔV from systemic velocity in km/s is given in the upper right corner. Synthesized beam is shown in the bottom left corner along with a 100 AU scale bar. The grey cross is centered on the star position and shows the position angle of the disk and maj/min axis ratio.

seemed to show significant asymmetry between the red-shifted and blue-shifted sides of the disk. We confirmed this by fitting each half of the disk separately. The fits only significantly differed in the stellar mass. One explanation for this asymmetry was an eccentric rather than a circular disk. Further evidence supporting a possible eccentric disk comes from the stellar mass we received from initial fits, $\sim 1 - 3M_\odot$. When compared to the spectral type of the star, K5 (Hillenbrand 1997), a significant portion of best-fit masses are much too large, even

when accounting for the fact that it is a pre-main-sequence star. We thus hypothesized that the system may be an unresolved tight binary, with a circumbinary disk. Previous studies have shown that circumbinary disks tend to be eccentric (Pelupessy & Portegies Zwart 2013).

Thus we modified our circular disk model and extended it to an eccentric disk. This requires the addition of two new parameters: the eccentricity (e) and the argument of periapsis (ω). Since the disk is no longer symmetric we must now model the disk in the full three dimensions. The radial bins from the circular model were transformed into semi-major axis bins, transforming the disk into N apsidally aligned elliptical wires with a single eccentricity for the entire system. Similar to the circular model, we would like to define a surface density profile by a power law with strength γ according to $\Sigma \propto r^{-\gamma}$; though we must now define it with respect to a , the semi-major axis, rather than simply the radius (note we remove the exponential tail used in the circular model). We can derive an expression for the mass of the i th ellipse, m_i , with semi-major axis a_i from the total disk mass M_{disk} :

$$m_i = \frac{M_{\text{disk}}}{a_i^\gamma} \left(\sum_{j=1}^N a_j^{-\gamma} \right)^{-1}. \quad (4.15)$$

We then spread out this mass along each ellipse according to how much time is spent on a Keplerian orbit with the given parameters. The density per unit length of each elliptical wire, λ_i , as a function of ϕ , the angle from periapsis, is then given by:

$$\lambda_i(\phi) = \frac{m_i \sqrt{1 - e^2}}{2\pi a_i (1 + e \cos \phi)}. \quad (4.16)$$

This linear density is then spread out between adjacent ellipses to get a surface

density:

$$\Sigma(\phi) = \frac{\lambda_i(\phi)}{(r_{i+1}(\phi) - r_{i-1}(\phi))/2}. \quad (4.17)$$

The radial coordinate can be obtained from the semi-major axis, eccentricity and angle ϕ by the polar equation for an ellipse:

$$r_i(\phi) = \frac{a_i(1 - e^2)}{1 + e \cos \phi} \quad (4.18)$$

As the velocity of an elliptical orbit is no longer entirely in the $\hat{\phi}$ direction, we must also modify the velocity profile. Again we assume a cylindrically rotating disk $v_z = 0$. If we define a cartesian coordinate system with the origin at the star, the x axis along the major axis, and periapsis in the positive x-direction, the x and y components of the velocity field are given by

$$\begin{aligned} v_{x,i}(\phi) &= -a_i \sqrt{\frac{GM_*}{a_i^3(1 - e^2)}} \sin \phi \\ v_{y,i}(\phi) &= a_i \sqrt{\frac{GM_*}{a_i^3(1 - e^2)}} (e + \cos \phi) \end{aligned} \quad (4.19)$$

These velocities can then be rotated according to the angle of periapsis, ω , and projected onto the line of sight vector according to the inclination of the disk to obtain a radial velocity. We did not implement any pressure term in the velocity field, as in the circular model. This term is already small ($\sim 1\%$ of the Keplerian velocity for a temperature of 30 K at 500 AU, Rosenfeld et al. 2013) and, since we are no longer implementing an exponential tail in the surface density profile, its effects become even less significant as the pressure gradient is not as steep. Figure 4.11 shows the modified velocity fields and surface density profile.

We did not modify the temperature profile from the original circular model.

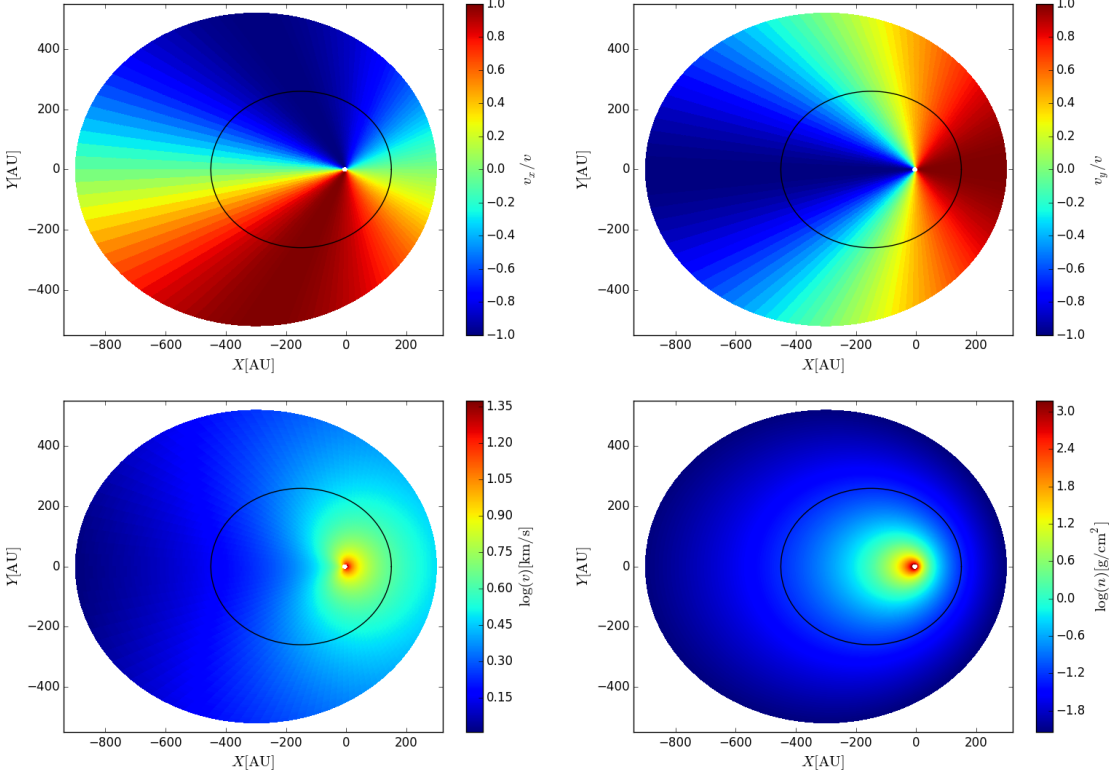


Figure 4.11: Top down views of a model eccentric disk with outer semi-major axis of 600 AU, eccentricity of 0.5, and disk mass of $0.09 M_{\odot}$. While an eccentricity of 0.5 is large, it is used in order to accentuate the differences between this elliptical model and a circular model. The mass of the star is $2 M_{\odot}$. Top: X (left) and Y (right) components of the elliptical Keplerian velocity profile normalized by the magnitude of the velocity field. Bottom: magnitude of the Keplerian velocity field (left) and surface density of the disk(right). Black ellipse is shown at a semi-major axis of 300 AU for reference.

It is worth mentioning that the position offset, $\Delta\alpha$ and $\Delta\delta$, must be allowed to vary when fitting the elliptical model, as the centroid of flux is no longer the position of the star. Since the asymmetry we were seeing in our residuals was due to an incorrect systemic velocity caused by the high velocity feature discussed in Section 5.6, we did not end up using this model in our fits. Once the code is fully operational, it will be useful in future projects as we observe more and more disks at greater resolution, enabling us to detect subtler asymmetries.

Chapter 5

Discussion

5.1 Planet-Forming Potential

In order to gauge the planet-forming potential of a protoplanetary disk, we use a theoretical minimum mass protoplanetary disk, from which the solar system could have formed from, called the minimum mass solar nebula (MMSN, Weidenschilling 1977, As discussed in Section 1.1). Once again, the MMSN is by no means the minimum mass *planet-forming* disk, though it does give us a lower baseline for how much mass would need to be available to form a planetary system like our own.

Figure 5.1 shows our best fit radial surface density profile derived from fitting the HCO⁺ and CO emission separately and together (see Tables 4.2 and 4.3 for the best fit parameters). As the CO emission is optically thick, it provides only a lower limit for the disk mass and thus a lower limit for the surface density. This is because optically thick emission comes from the $\tau = 1$ surface and gas below that surface is hidden. Also, due to cloud contamination, we were able to fit only the high velocity red-shifted emission. This resulted in a relatively unconstrained critical radius. The combination of a lower limit on the disk mass and unconstrained critical radius make the median CO profile meaningless and thus we show only the best fit model. In all fits the surface density power-law index γ was fixed at 1. Since we also fixed the disk mass in our two-line fits, the only parameters which were allowed to vary and affect the surface density profile

were the critical radius R_c and the HCO^+ fractional abundance X_{HCO^+} . We fixed the mass at $0.045 M_\odot$, the mass estimated from continuum observations by Mann et al. (2014); Mann & Williams (2010, 2009a). Since the CO(3–2) emission constrained q to a more reasonable value of -0.24 ± 0.02 , compared to the best fit to the $\text{HCO}^+(4–3)$ emission of 0.07 ± 0.07 , the critical radius was pushed to an extremely large value to increase the flux in the outer disk in $\text{HCO}^+(4–3)$. This decreases the surface density of the entire disk by pushing mass into the outer disk. Our best fit surface density profiles derived from fitting individual lines pass through the MMSN surface density ranges, while the profile of the two-line fit is slightly below the MMSN, due to the larger size. Our best fit disk masses, however, are well above the total mass of the MMSN. This demonstrates that d216-0939 has sufficient mass to represent significant planet-forming potential.

Also shown in Figure 5.1 is the median profile for interferometrically resolved disks in Ophiuchus presented by Andrews et al. (2009, 2010) (only continuous disks, not those showing an inner cavity). Our profiles, derived from fitting individual lines, are similar to this profile. With the caveat that this is a sample size of one, this similarity reveals that the planet-forming environment in Ophiuchus and the outskirts of Orion are similar (this disk is located 1.6 projected pc north of θ^1 Ori C). Thus we can safely apply what we have learned from studies of disks in low-mass SFR’s like Taurus and Ophiuchus to isolated disks in Orion.

5.2 Dynamical Mass of a Pre-Main Sequence Star

Since a star’s mass determines its evolutionary path through the HR-diagram, it can tell us about properties of the star and its formation. Unfortunately, determining the mass of a star is difficult, and a pre-main sequence star is even

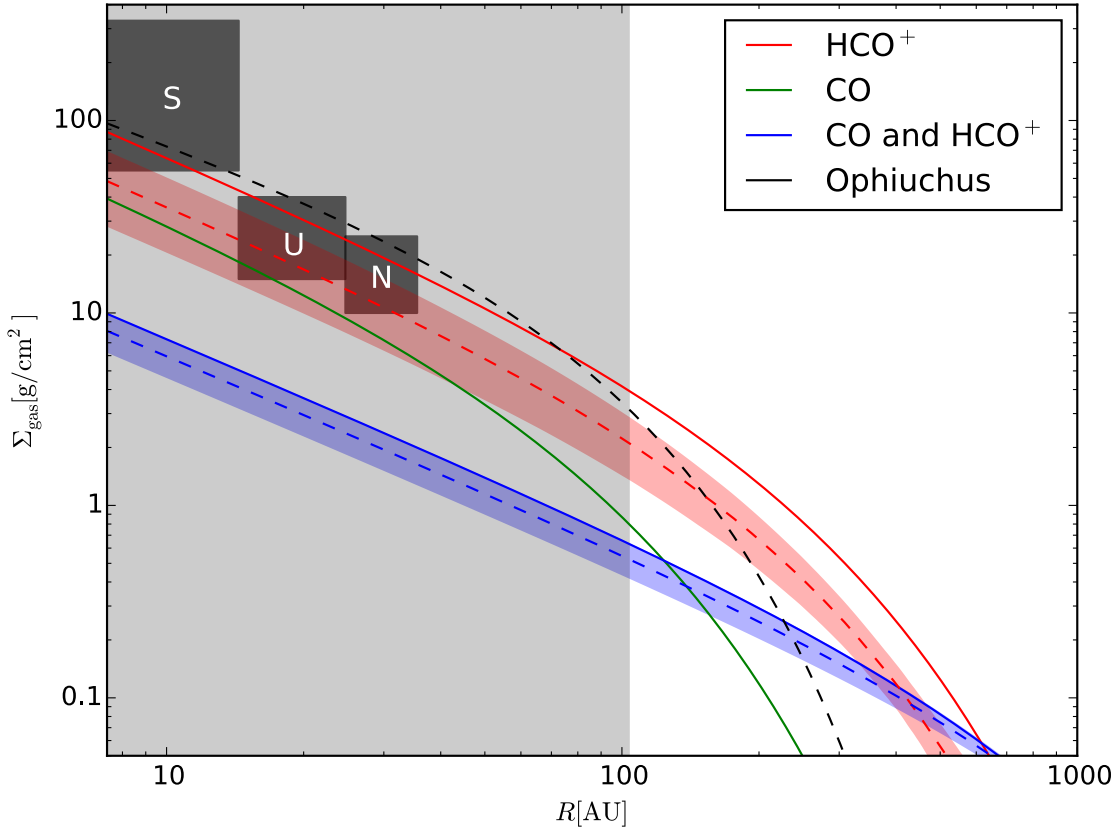


Figure 5.1: Radial surface density profiles derived for d216-0939 using HCO^+ (red), CO (green) and the two lines together (blue) alongside the median profile for disks in Ophiuchus (black) given by Andrews et al. (2009, 2010) ($M_{\text{disk}} = 0.06M_{\odot}$, $\gamma = 0.8$, $R_c = 85$ AU). Profiles of best fit models are shown with solid lines while median profiles are shown with dashed lines with 1σ error bars shaded. CO emission provides a lower limit on the disk mass; thus the median profile for CO is not shown. The dark grey rectangular regions mark the surface densities for Saturn, Uranus, and Neptune in the Minimum Mass Solar Nebula (Weidenschilling 1977). The light grey region marks the resolution limit of the ALMA observations.

more so. The most accurate way to measure the mass of an astronomical object is to examine orbit of a satellite of that object. This is impossible to do for a typical star. We must then use a derived mass from the color/temperature of the star and any other information we have on the system such as metallicity and age. Ultimately these estimates are tied to eclipsing binary systems where we can correlate the mass and temperature of stars. While these values are relatively accurate for main sequence stars, many more assumptions go into simulations of pre-main sequence stars such as accretion, magnetic fields, and rotation. Thus our understanding of pre-main sequence evolution is limited by our over-simplified models. An accurate determination of the mass of a pre-main sequence star can help to calibrate pre-main sequence evolutionary tracks and help determine the age of the Orion Nebula Cluster.

Determining the stellar mass from molecular line observations of a circumstellar disk in the radio frequency domain is relatively simple. As discussed in Section 4.1, we assume a Keplerian velocity profile which we can then fit to the data. The two unknowns in calculating this profile are the distance to the system, which affects the conversion of angular to spatial scales, and the inclination, which affects the projection of the rotational velocity onto the line of sight. If the disk is spatially resolved, the inclination should be well constrained by the ratio of major to minor axes of the elliptical image (assuming a circular disk). The distance to the Orion Nebula has been well constrained using the Very Long Baseline Array to measure parallactic distances. Sandstrom et al. (2007) measured a distance of 389_{-21}^{+24} pc while Menten et al. (2007) measured a distance of 414 ± 7 pc. The distance was also measured at 410 ± 20 pc and 392 ± 34 pc by Kraus et al. (2009) and Jeffries (2007), respectively. We have used a distance of 400 pc in this work, while the weighted average of the previously stated values is 410 ± 6 pc. This

corresponds to a 1.5% uncertainty in the distance which translates directly to an additional 1.5% uncertainty on the estimated mass. Rosenfeld et al. (2012a) provides an in depth analysis of the procedure we emulate in this work. As they observed a disk around a binary star, they also compared their disk derived mass to radial velocity measurements and found excellent agreement.

Using our dynamical mass measurement and an effective temperature, we can determine an age and luminosity of the star-disk system using a set of theoretical pre-main sequence evolutionary tracks. We first use the spectral type of the star, K5 (determined spectroscopically by Hillenbrand 1997, with an uncertainty of ± 0.5 for types earlier than K9), to estimate an effective temperature of 4400 K (Popper 1980; Boehm-Vitense 1981; Bell & Gustafsson 1989). We then place the star on a set of theoretical pre-main sequence tracks using the estimated temperature and our best fit M_* of $2.08 \pm 0.05 M_\odot$. This allows us to estimate the age of the system based on where the temperature intersects with the stellar mass. Given the stated uncertainty of the spectral classification and a review of the literature, we estimate an error in the temperature of 200 KK. Figure 5.2 shows evolutionary tracks presented by Palla & Stahler (1999) for the Orion Nebula Cluster along with our assumed effective temperature. The $2 M_\odot$ evolutionary track *does not* intersect with the assumed effective temperature within 1σ . This could be due to an incorrect determination of the spectral type of the star or inaccuracies in the evolutionary tracks. Observations by Smith et al. (2005) using HST showed the disk to be inclined at approximately the flaring angle. This causes a large reflection nebula to the east and extinction of the star caused by the disk, both of which could affect the spectral classification and definitely the observed luminosity.

This hypothesis is supported by the extremely old age of the system, 66 Myr

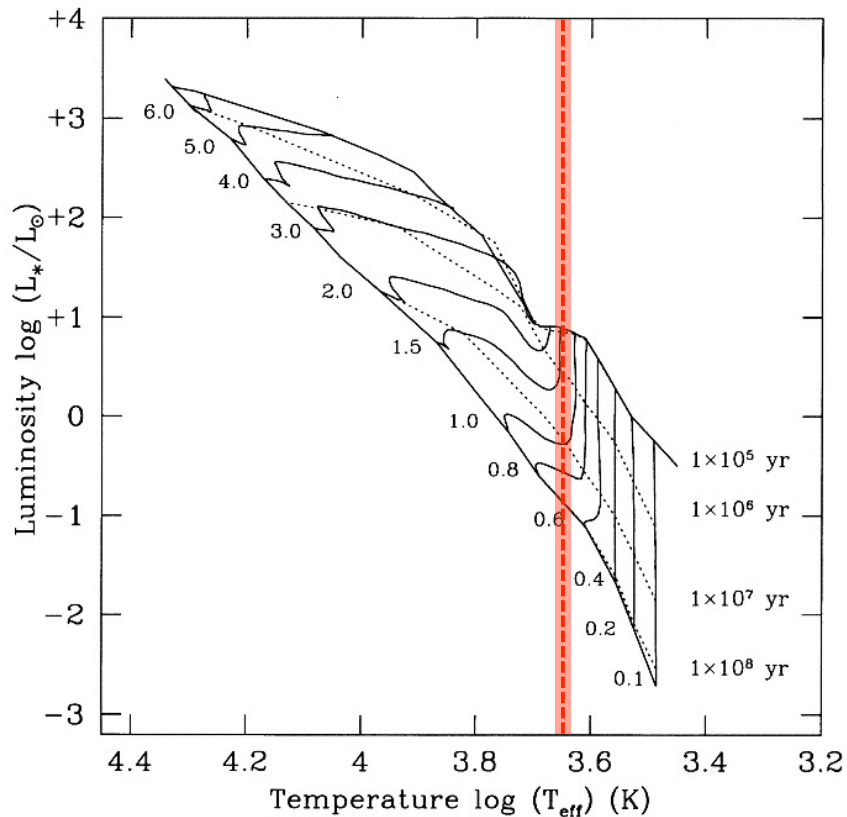


Figure 5.2: Theoretical pre-main sequence tracks in the H-R diagram. Each track is labeled by the corresponding stellar mass, in units of M_\odot . Selected isochrones are shown by the dotted lines. For each track, the evolution starts at the birthline (light solid line), and ends at the ZAMS, also indicated. Caption and Figure reproduced from fig. 1 of Palla & Stahler (1999). Vertical red dashed line and shaded area indicates the effective temperature and uncertainty of 216-0939, as derived from the spectral type.

derived by Hillenbrand (1997). This age is almost two orders of magnitude older than their own derived age of the Orion Nebula Cluster (<1 Myr with a 2 Myr spread). Our observations of a gas-rich protoplanetary disk solidly limit the age of the system to $\lesssim 10$ Myr and most likely closer to $\lesssim 1-2$ Myr. Stellar ages derived by Hillenbrand (1997) were calculated by comparing the effective temperature (derived from the spectral type) and the observed magnitude (converted to stellar luminosity) to pre-main sequence isochrones. Thus, if the observed magnitude was fainter than the true magnitude due to extinction by the inclined disk, the derived age would be much older than the true age.

A more accurate spectral classification of this star, taking into account any effects the disk may have, combined with our mass measurement, will give the theorists a datapoint to calibrate their models to. It will also allow us to determine the age of the system by its place on a theoretical pre-main sequence evolutionary track, and

5.3 Best Fit Temperature Structure

Comparing the two single line fits, we can see a few interesting trends in the temperature profiles (best fit parameters are given in Tables 4.2 and 4.3). First, the atmospheric temperature of our best fit to only the HCO⁺ emission is an unreasonably cold 22 K. To compensate for the extremely cold atmospheric temperature, q (the radial temperature power-law index) has been pushed close to zero (and even greater than zero in our median fit), in order to increase emission in the outer disk. The expected value for q in a geometrically flat, optically thin disk is -0.5 while measured values vary from -0.6 to -0.3 (Dartois et al. 2003; Rosenfeld et al. 2012a,b) due to the flared structure of the disk and high optical

depth. Our best fit value when fitting only the CO line matches nicely with these values. The best fit atmospheric temperature for the CO line fit is 41_{-3}^{+5} K, much more reasonable than that of HCO^+ . This discrepancy is due to the fact that the $\text{HCO}^+(4-3)$ and $\text{CO}(3-2)$ emission originate from different regions of the disk. Since $\text{HCO}^+(4-3)$ is optically thin it stems from the cold interior. On the other hand, $\text{CO}(3-2)$ is optically thick and thus we see the only the $\tau = 1$ surface which is presumably higher up in the disk and thus hotter. There is also a degeneracy between temperature and density in the optically thin $\text{HCO}^+(4-3)$ line (as seen in the triangle plot shown in Figure 4.3). Multi-line fitting is required to break this degeneracy.

The temperature structure of our best fit to the CO and HCO^+ emission together is significantly warmer than both single line fits. The CO snow line (19 K) falls at a radius of 425 AU (though this value is model dependent), consistent with the location we would expect for a blackbody equilibrium temperature of a $4 L_\odot$ star. Using the pre-main sequence evolutionary tracks of Palla & Stahler (1999) (Figure 5.2, presented in Section 5.2) this is consistent with a $2 M_\odot$, 1 Myr old star, similar to our best fit mass and assumed age.

The height parameter $z_{q,150}$ is much larger than the value we fixed it at in the single line fits, which corresponded to $z_q \simeq 2H$ where H is the scale height of the disk. Since the disk as a whole is warmer than the best fit single line models, the scale height is larger.

5.4 HCO^+ Abundance Structure

As outlined in Section 4.1 we use a constant fractional abundance throughout the disk for all gas species (with the exception of freeze-out and photodissociation

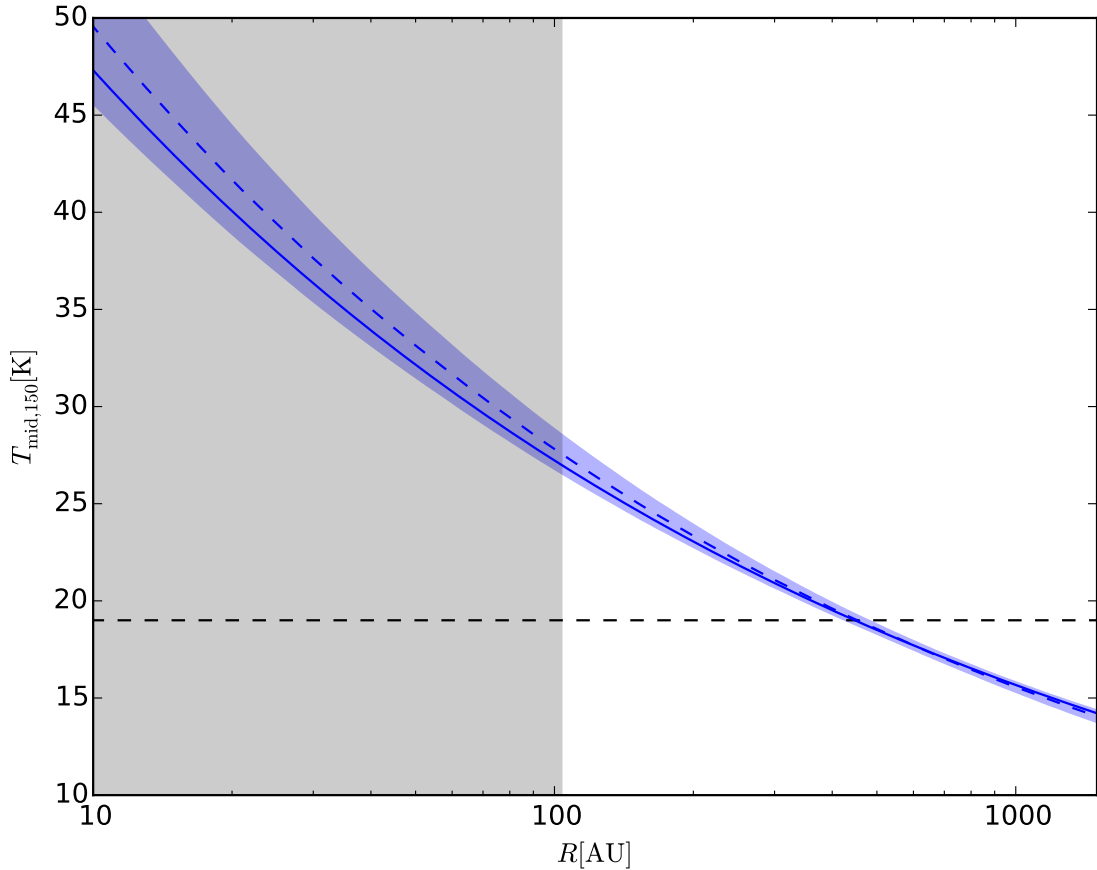


Figure 5.3: Radial midplane temperature profile derived for d216-0939 using the $\text{HCO}^+(4-3)$ and $\text{CO}(3-2)$ lines together. The best fit model is shown with a solid line while median profile is shown with a dashed line, with 1σ error bars shaded. The freezeout temperature of CO (19 K, Qi et al. 2011) is indicated by the black dashed line. The light grey region marks the resolution limit of the ALMA observations.

effects). While this is a reasonable assumption for CO, the chemistry of HCO⁺ causes its structure to be much more complicated. Cleeves et al. (2014) and Walsh et al. (2013) have both simulated the chemistry in protoplanetary disks with different levels of ionization (ether from external sources or the central star). Using a simple set of initial conditions, they evolve the disk by simulating a chemical network consisting of 5910 and 43366 reactions and 639 and 378 species, respectively. Both studies produce a vertical HCO⁺ fractional abundance profile which, with increasing height, increases by several orders of magnitude, then decreases again. The fractional abundances relative to H₂ peak at 10⁻⁹ and 10⁻⁶, respectively.

While the vertical CO abundance does follow a similar profile due to freeze-out in the midplane and photoionization near the disk surface, the profile is much more complicated and exaggerated in HCO⁺ due to the chemical reactions and ionization which produce the species. The profile also narrows (with respect to height) with increasing levels of ionization. In simulations by Cleeves et al. (2014), the HCO⁺ fractional abundance even showed a two-layered structure with the main peak coincident with the peak of the CO progenitor gas and a weak secondary peak near the surface of the disk where the ionization rate was higher. In the future, we may experiment with implementing a vertical gradient in the HCO⁺ abundance to more accurately model the theorized structure of HCO⁺. Since the vertical structure of this disk is not spatially resolved, we may not be able to constrain this vertical structure.

5.5 Rough Characterization of Ionizing Radiation Level

Walsh et al. (2013) modeled the structure and emission from a disk surrounding

a T Tauri star, being irradiated by a nearby O star and compared the gas line emission to that from an isolated disk. They found that, in general, line emission from the irradiated disk showed higher peak values due to the warmer disk. This was not the case for HCO^+ which traces the cold, dense areas of the disk. Thus, the ratio of the HCN/HCO^+ peak intensities can be used to roughly characterize the level of external irradiation, with $\text{HCN}/\text{HCO}^+ > 1$ indicating an irradiated disk and $\text{HCN}/\text{HCO}^+ < 1$ characteristic of an isolated disk. They also predicted that transitions of CO, ^{13}CO , C^{18}O , CI, HCO^+ , HCN and CN would be observable at the distance of Orion, with CS and C_2H possibly observable in larger, more massive disks.

Since d216-0939 is relatively isolated, we do not expect it to be highly irradiated. We measure the ratio of HCN/HCO^+ peak flux (peak flux values are presented in Chapter 3) to be 0.58 ± 0.04 , comparable to the isolated model given by Walsh et al. (2013). This is not a surprising result given the location of the disk (isolated and 1.6 pc north of θ^1 Ori C). We also support the predictions the authors made about certain lines being observable, with our detection of CO, HCO^+ , HCN, and CS. Our detection of CS supports their prediction that CS would be observable in larger, more massive disks, since d216-0939 is the largest and one of the most massive disks observed in Orion (Mann & Williams 2009a). We also note that, while we did not model the emission, our HCN(4-3) maps are free of cloud contamination. Consequently, HCN may be a good disk tracer for observations in regions with contamination in CO or HCO^+ , especially closer to bright high mass stars, as the line was shown to grow in intensity.

5.6 High Velocity Asymmetry

As previously discussed, we observe an excess of high velocity, blue-shifted, emission in CO(3–2), HCO⁺(4–3) and HCN(4–3). This feature is clearly visible in the HCO⁺(4–3) emission as a second peak in flux near the star and along the disk major axis at -6 km/s (relative to the systemic velocity), as seen in Figures 3.5 and 3.6. The feature exceeds 5σ in 3 channels (emission does not go below 3σ between the disk and the feature). We excluded these channels from our fits, initially attributing the emission to an accretion stream, an outflow, or some other more complicated inner disk process. Residuals from fitting a symmetric model to the CO(3–2) emission showed the same feature, though spectrally wider.

Fitting an elliptical Gaussian to the residual visibilities results in a position offset of 0.11 ± 0.03 arcsec north of star, along the major axis of the disk, corresponding to a projected linear offset of 46 ± 10 AU (the feature is not resolved so the size cannot be determined). We can then compare the observed velocity of the peak to a Keplerian orbit at the measured position offset. The line of sight velocity of such an orbit (using the best fit parameters for stellar mass and inclination from the HCO⁺ line only fits) at the measured position offset is -6.2 ± 0.8 km/s.

In order to measure the exact spectral location of the feature we fit a Gaussian to the spectrum generated (using the MIRIAD task `imspec`) from the residual emission. The peak is located at 5.95 km/s in HCO⁺ and 6.08 km/s in CO, which agree with each other within our channel spacing of 0.42 km/s. We also go the other direction and calculate an orbital radius of 45 ± 3 AU from the velocity of the emission peak. All of these values are well within 1σ of each other. We thus conclude that the emission is caused by a local density, temperature, and/or

scale-height enhancement in the inner disk and not due to a separate dynamical process that would deviate from a Keplerian velocity profile.

Since the feature is unresolved, we cannot determine the structure of the feature. We can, however, use the spectral extent to estimate the radial extent of the feature, and the integrated flux to determine the mass of the emitting gas. The Gaussian fit to the spectrum of the feature allowed us to determine not only the velocity of the peak emission but also the spectral extent. We derived a FWHM of 0.94 and 4.95 km/s for the HCO⁺(4–3) and CO(3–2) emission, respectively. We also determined the density enhancement needed to produce such a feature by comparing the peak flux (from the Gaussian fit) to the flux of our best fit model at the same velocity. We derived a 10× and 2× enhancement in HCO⁺(4–3) and CO(3–2), respectively. The fact that HCO⁺(4–3) traces denser gas than CO(3–2), and CO(3–2) is optically thick may be causing the discrepancy between the two lines' spectral extent and density enhancement. HCO⁺(4–3) would trace the core of the cloud, making it much more compact and dense, while CO(3–2) would trace the outskirts, making it extended and less dense since mass would be hidden under the $\tau = 1$ surface.

Finally, we estimated a gas mass of the feature using the optically thin HCO⁺(4–3) emission. We determined the integrated flux in the line using the MIRIAD task `cgcurs` to measure the intensity in the zeroth moment map (of the residuals in channels corresponding to velocities ≤ -5.1 km/s relative to systemic velocity) above the 3σ level. Using Equation 3.1 and the best fit HCO⁺ abundance and atmospheric temperature of the disk (see Equation 4.2 and Table 4.3) at the radius of the feature, we calculate a gas mass of $9 \pm 4 M_{\text{Jupiter}}$. Using the midplane temperature, instead of the atmospheric temperature, results in a mass of $6 \pm 2 M_{\text{Jupiter}}$. Since the excitation temperature changes with height inside the disk,

the actual mass may be somewhere in-between these two values. It could also be much hotter if, for example, the temperature was locally raised by accretion luminosity from the forming protoplanet. Again, this mass is highly dependent on the abundance of HCO⁺ relative to H₂, which is somewhat uncertain.

In general, protoplanetary disks tend to be azimuthally, and thus spectrally, symmetric. Thus any deviation from symmetry tells us that something interesting is going on. Since we observe disks in order to study planet formation, an exciting and not extraordinary conclusion for the cause of any asymmetric features would be the presence of a planet or a step in the process of planet formation (or destruction). While this is a possibility, there are a few other causes for asymmetry in disks which are not related to planets.

The first is a recent collision similar to that described by Telesco et al. (2005). Multi wavelength observations of the continuum which resolve this feature could tell us about the grain sizes present in the feature and could help determine the dynamical process causing the enhancement. Another possibility is a stellar flyby which could disrupt the disk (Reche et al. 2009). It is not likely that this is the cause of this particular feature as it is located in the inner disk and a stellar flyby should preferentially perturb the outer disk, which we do not see. The nearest star is ~ 4 arcsec (1600 AU) to the south west and could be a distant companion, though this has not been confirmed (J. Bally, private communication). A third possible cause are zonal flows caused by interactions between disk material and a magnetic field. This magneto-rotational instability (MRI) causes pressure and density fluctuations which can cause asymmetries in emission (Flock et al. 2015). These density enhancements are thought to be regions which could promote grain growth and planetesimal formation (Dittrich et al. 2013). Our observations are not high enough resolution to investigate turbulence caused by MRI and thus we

cannot determine the viability of this mechanism.

While there are many possible explanations for the origin of the asymmetry we see, one in particular, stands out. Since HCO^+ is a good tracer of dense gas due to its high critical density, Narayanan et al. (2006) simulated observations of planet formation in a gravitationally unstable protoplanetary disk. They conclude that $\text{HCO}^+(7-6)$ can be used to trace gas giant planet formation through gravitational instabilities and the signature would be observable with ALMA. The high velocity feature we see in our observations is similar to that which they describe, though in a lower transition of HCO^+ . Unfortunately d216-0939 is not nearly massive enough to exhibit gravitational instability ($\gtrsim 10\%$ of host star mass). The Toomre Q parameter, given by

$$Q \equiv \frac{c_s \Omega}{\pi G \Sigma}, \quad (5.1)$$

can be used to determine the gravitational stability of a disk (Toomre 1964); where c_s is the sound-speed given by Equation 4.5, Ω is the orbital frequency, G is the gravitational constant, and Σ is the surface density. A disk is stable when $Q > 1$ and unstable otherwise. Figure 5.4 shows the Toomre Q parameter plotted as a function of radius for our 3 best fit models. Since c_s depends on temperature, we have plotted a range of Q 's corresponding to the mid-plane and atmospheric temperatures. Although d216-0939 is not gravitationally unstable, the possibility that the feature we observe could be the signature of a significant density enhancement around a forming gas giant planet is not ruled out, only that the planet is forming through the process of gravitational instability.

If this feature does correspond to a planet in the early stages of formation, it would be the first time such a signature has been detected. This feature warrants follow-up observations using ALMA's newly commissioned long baselines to better

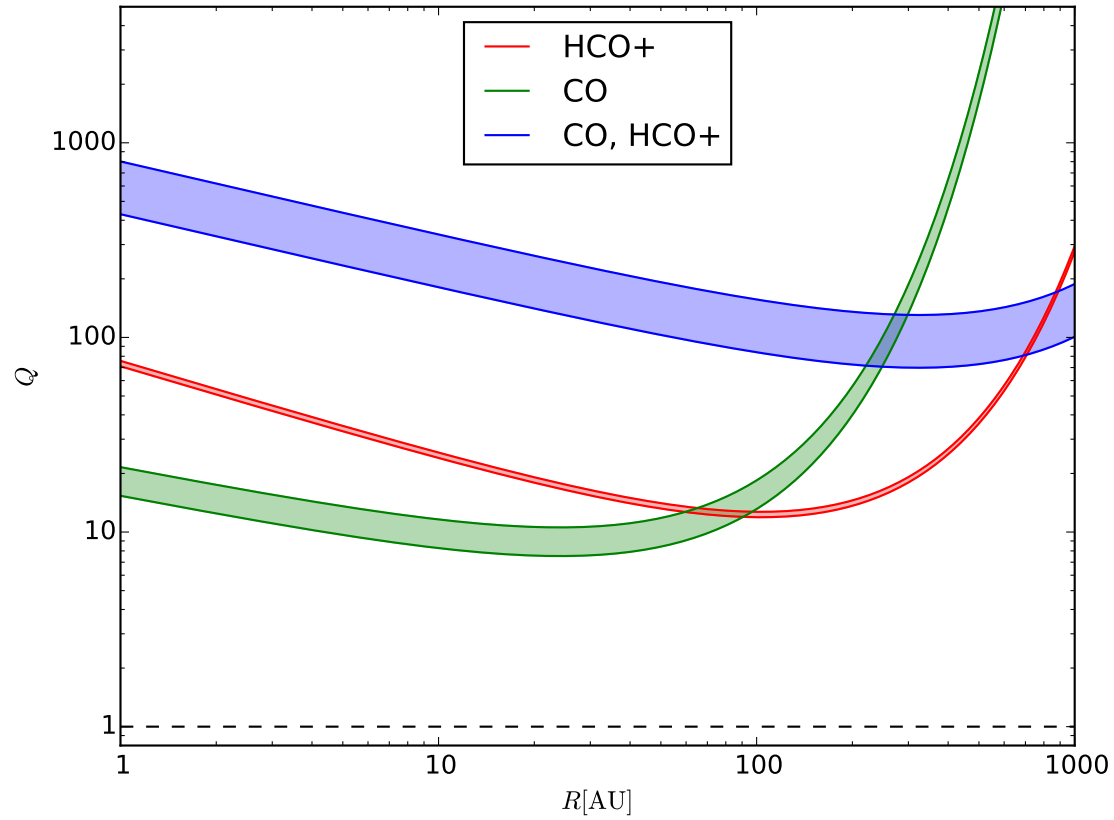


Figure 5.4: Toomre Q parameter given in Equation 5.1 as a function of radius for our 3 best fit models. As our disk is not isothermal, a range is shown using the mid-plane and atmospheric temperatures. The dashed line shows the instability threshold such that $Q < 1$ is unstable.

constrain its properties and thus its source.

Chapter 6

Summary

In this work, we have presented spatially and spectrally resolved observations of the HCO⁺(4–3), HCN(4–3), CO(3–2), and CS(7–6) transitions from the protoplanetary disk d216-0939 located in the Orion Nebula Cluster (ONC). We defined a gas model assuming Keplerian rotation and local thermodynamic equilibrium. We then used an affine invariant MCMC algorithm to fit our model to the HCO⁺(4–3) and CO(3–2) transitions and statistically characterized the temperature and density structure of the disk as well as the mass of the central star.

Our best fit parameters are consistent with typical massive disks in Taurus and ρ Ophiuchus. This demonstrates that disks in the ONC, a high-mass star forming region (SFR), which are far enough away from θ^1 Ori C not to be externally photoevaporated, can show significant planet forming potential. Our best fit disk mass is greater than the previous dust continuum measurements by Mann & Williams (2009a) and Mann et al. (2014), though these previous measurements were lower limits since they assumed a gas to dust ratio of 100:1 and large bodies are invisible to submillimeter observations and could hide a significant amount of mass. Since we could not use the optically thick CO(3–2) emission to constrain the disk mass, our measurement is inherently tied to the HCO⁺ fractional abundance, which has significant associated uncertainties. In the future, we will also model the HCN(4–3) line to further constrain the temperature and density structure. We may also model the structure of the HCO⁺ abundance, as it has been shown to be more complicated than CO.

We measured a mass of the central star by modeling the Keplerian rotation

of the disk. This dynamical mass estimate of $2.08 \pm 0.05 M_{\odot}$ is inconsistent with the spectral type of K5 measured by Hillenbrand (1997). This could be due to contamination from the highly inclined disk or simply inaccuracies in fitting spectral types to pre-main sequence stars and the temperatures associated with each type. In the latter case, our measurement defines a datapoint from which future models may be calibrated.

While the disk structure was the main goal of this work, we serendipitously uncovered a surprising and intriguing feature in our observations. Excess high-velocity blue-shifted emission was detected, though not resolved, in all lines except CS(7–6). The spatial and spectral position of this feature indicate that it is consistent with a Keplerian orbit at 45 ± 8 AU. Using the integrated flux of the feature in $\text{HCO}^+(4-3)$ and our best fit temperature structure, we estimate a gas mass of $7 \pm 3 M_{\text{Jupiter}}$ in the feature. Narayanan et al. (2006) have shown that a gas giant planet forming through gravitational instability could be detected using ALMA in high density tracers such as $\text{HCO}^+(7-6)$. While our observations are of $\text{HCO}^+(4-3)$ and this disk is not gravitationally unstable, it is possible that we have detected a gas giant planet in the early stages of formation. It is also possible that this feature may simply be a density enhancement caused by some other mechanism, though our observations do not resolve the feature and thus we cannot be certain. This feature warrants follow-up observations.

In future work, we will model the $\text{HCN}(4-3)$ emission, in addition the two lines presented here, to further constrain the temperature and density structure of this disk. The addition of another line will allow us to vary more parameters which were unconstrained or highly degenerate when only fitting two lines. We will also be able to more accurately determine the mass in the previously discussed asymmetric feature with the addition of $\text{HCN}(4-3)$.

References

- Aikawa, Y., & Herbst, E. 1999, *A&A*, 351, 233
- ALMA Partnership et al. 2015, ArXiv e-prints, 1503.02649
- Andrews, S. M., & Williams, J. P. 2005, *ApJ*, 631, 1134
- . 2007, *ApJ*, 671, 1800
- Andrews, S. M., Wilner, D. J., Hughes, A. M., Qi, C., & Dullemond, C. P. 2009, *ApJ*, 700, 1502
- . 2010, *ApJ*, 723, 1241
- Bally, J., Sutherland, R. S., Devine, D., & Johnstone, D. 1998, *AJ*, 116, 293
- Beckwith, S. V. W., Sargent, A. I., Chini, R. S., & Guesten, R. 1990, *AJ*, 99, 924
- Bell, R. A., & Gustafsson, B. 1989, *MNRAS*, 236, 653
- Bergin, E. A., et al. 2013, *Nature*, 493, 644
- Boehm-Vitense, E. 1981, *ARA&A*, 19, 295
- Brinch, C., & Hogerheijde, M. R. 2010, *A&A*, 523, A25
- Butler, B. 2012, ALMA Memo 594
- Churchwell, E., Felli, M., Wood, D. O. S., & Massi, M. 1987, *ApJ*, 321, 516
- Cleeves, L. I., Bergin, E. A., & Adams, F. C. 2014, *ApJ*, 794, 123
- Cornwell, T. J., & Evans, K. F. 1985, *A&A*, 143, 77
- Da Rio, N., Robberto, M., Soderblom, D. R., Panagia, N., Hillenbrand, L. A., Palla, F., & Stassun, K. 2009, *ApJS*, 183, 261
- Dartois, E., Dutrey, A., & Guilloteau, S. 2003, *A&A*, 399, 773
- Dittrich, K., Klahr, H., & Johansen, A. 2013, *ApJ*, 763, 117
- Drabek, E., et al. 2012, *MNRAS*, 426, 23
- Flock, M., Ruge, J. P., Dzyurkevich, N., Henning, T., Klahr, H., & Wolf, S. 2015, *A&A*, 574, A68

- Fogel, J. K. J., Bethell, T. J., Bergin, E. A., Calvet, N., & Semenov, D. 2011, *ApJ*, 726, 29
- Foreman-Mackey, D., Hogg, D. W., Lang, D., & Goodman, J. 2013, *PASP*, 125, 306
- Fressin, F., et al. 2013, *ApJ*, 766, 81
- Gaidos, E., Krot, A. N., Williams, J. P., & Raymond, S. N. 2009, *ApJ*, 696, 1854
- Goodman, J., & Weare, J. 2010, Comm. App. Math. and Comp. Sci, 5, 65
- Hartmann, L., Calvet, N., Gullbring, E., & D'Alessio, P. 1998, *ApJ*, 495, 385
- Henney, W. J., & O'Dell, C. R. 1999, *AJ*, 118, 2350
- Hernández, J., Hartmann, L., Calvet, N., Jeffries, R. D., Gutermuth, R., Muze-rolle, J., & Stauffer, J. 2008, *ApJ*, 686, 1195
- Hildebrand, R. H. 1983, *QJRAS*, 24, 267
- Hillenbrand, L. A. 1997, *AJ*, 113, 1733
- Högblom, J. A. 1974, *A&AS*, 15, 417
- Hubickyj, O., Bodenheimer, P., & Lissauer, J. J. 2005, *ICAR*, 179, 415
- Hughes, A. M., Wilner, D. J., Kamp, I., & Hogerheijde, M. R. 2008a, *ApJ*, 681, 626
- Hughes, A. M., Wilner, D. J., Qi, C., & Hogerheijde, M. R. 2008b, *ApJ*, 678, 1119
- Isella, A., Carpenter, J. M., & Sargent, A. I. 2009, *ApJ*, 701, 260
- Izidoro, A., Morbidelli, A., & Raymond, S. N. 2014, *ApJ*, 794, 11
- Jeffries, R. D. 2007, *MNRAS*, 376, 1109
- Kraus, S., et al. 2009, *A&A*, 497, 195
- Lada, C. J., & Lada, E. A. 2003, *ARA&A*, 41, 57
- Lynden-Bell, D., & Pringle, J. E. 1974, *MNRAS*, 168, 603
- Mann, R. K., et al. 2014, *ApJ*, 784, 82
- Mann, R. K., & Williams, J. P. 2009a, *ApJL*, 699, L55
- . 2009b, *ApJL*, 694, L36

- . 2010, *ApJ*, 725, 430
- McCullough, P. R., Fugate, R. Q., Christou, J. C., Ellerbroek, B. L., Higgins, C. H., Spinhirne, J. M., Cleis, R. A., & Moroney, J. F. 1995, *ApJ*, 438, 394
- Menten, K. M., Reid, M. J., Forbrich, J., & Brunthaler, A. 2007, *A&A*, 474, 515
- Narayanan, D., Kulesa, C. A., Boss, A., & Walker, C. K. 2006, *ApJ*, 647, 1426
- O'dell, C. R., & Wen, Z. 1994, *ApJ*, 436, 194
- Palla, F., & Stahler, S. W. 1999, *ApJ*, 525, 772
- Pavlyuchenkov, Y., Semenov, D., Henning, T., Guilloteau, S., Piétu, V., Launhardt, R., & Dutrey, A. 2007, *ApJ*, 669, 1262
- Pelupessy, F. I., & Portegies Zwart, S. 2013, *MNRAS*, 429, 895
- Popper, D. M. 1980, *ARA&A*, 18, 115
- Qi, C., D'Alessio, P., Öberg, K. I., Wilner, D. J., Hughes, A. M., Andrews, S. M., & Ayala, S. 2011, *ApJ*, 740, 84
- Reche, R., Beust, H., & Augereau, J.-C. 2009, *A&A*, 493, 661
- Reggiani, M., Robberto, M., Da Rio, N., Meyer, M. R., Soderblom, D. R., & Ricci, L. 2011, *A&A*, 534, A83
- Ricci, L., Mann, R. K., Testi, L., Williams, J. P., Isella, A., Robberto, M., Natta, A., & Brooks, K. J. 2011, *A&A*, 525, A81
- Ricci, L., Robberto, M., & Soderblom, D. R. 2008, *AJ*, 136, 2136
- Rosenfeld, K. A., Andrews, S. M., Hughes, A. M., Wilner, D. J., & Qi, C. 2013, *ApJ*, 774, 16
- Rosenfeld, K. A., Andrews, S. M., Wilner, D. J., & Stempels, H. C. 2012a, *ApJ*, 759, 119
- Rosenfeld, K. A., et al. 2012b, *ApJ*, 757, 129
- Sandstrom, K. M., Peek, J. E. G., Bower, G. C., Bolatto, A. D., & Plambeck, R. L. 2007, *ApJ*, 667, 1161
- Schöier, F. L., van der Tak, F. F. S., van Dishoeck, E. F., & Black, J. H. 2005, *A&A*, 432, 369
- Skilling, J., & Bryan, R. K. 1984, *MNRAS*, 211, 111

- Smith, N., Bally, J., Licht, D., & Walawender, J. 2005, *AJ*, 129, 382
- Strom, K. M., Strom, S. E., Edwards, S., Cabrit, S., & Skrutskie, M. F. 1989, *AJ*, 97, 1451
- Tachibana, S., Huss, G. R., Kita, N. T., Shimoda, G., & Morishita, Y. 2006, *ApJL*, 639, L87
- Telesco, C. M., et al. 2005, *Nature*, 433, 133
- Toomre, A. 1964, *ApJ*, 139, 1217
- Tsiganis, K., Gomes, R., Morbidelli, A., & Levison, H. F. 2005, *Nature*, 435, 459
- Vicente, S. M., & Alves, J. 2005, *A&A*, 441, 195
- Walsh, C., Millar, T. J., & Nomura, H. 2013, *ApJL*, 766, L23
- Walsh, K. J., Morbidelli, A., Raymond, S. N., O'Brien, D. P., & Mandell, A. M. 2011, *Nature*, 475, 206
- Weidenschilling, S. J. 1977, *Ap&SS*, 51, 153
- Weintraub, D. A., Sandell, G., & Duncan, W. D. 1989, *ApJL*, 340, L69
- Wernecke, S., & D'Addario, L. 1977, Computers, IEEE Transactions on, C-26, 351
- Williams, J. P., & Best, W. M. J. 2014, *ApJ*, 788, 59
- Williams, J. P., & Cieza, L. A. 2011, *ARA&A*, 49, 67